SYNTHESIS AND ELECTRICAL CHARACTERIZATION OF BISMUTH FERRITE THIN FILMS

By

Hamidreza Khassaf

Submitted to Graduate School of Engineering and Natural Sciences

in Partial Fulfillment of the Degree of

Master of Science

Sabancı University

August 201

SYNTHESIS AND ELECTRICAL CHARACTERIZATION OF BISMUTH FERRITE THIN FILMS FABRICATED THROUGH SOL-GEL METHOD

APPROVED BY:

Asst. Prof. İ. Burç Mısırlıoğlu ....

(Thesis Supervisor)

Assoc. Prof. Cleva Ow-Yang ....

Assoc. Prof. Mehmet Ali Gülgün ....

Asst. Prof. Dr. Gözde İnce ....

Assoc. Prof. Ali Koşar ....

Assoc. Prof. Dr. Mehmet Yıldız ....

DATE OF APPROVAL: 1/8/2012

© Hamidreza KHASSAF 2012

All Rights Reserved

SYNTHESIS AND ELECTRICAL CHARACTRIZATION OF BISMUTH FERRITE THIN FILMS

Hamidreza Khassaf

Material Science and Engineering, M.Sc. Thesis, 2012

Thesis Supervisor: Assist. Prof. İ. Burç Mısırlıoğlu

Keywords: Ferroelectrics, bismuth ferrite, epitaxial growth, chemical solution deposition (CSD), spin coating, potential barrier, Gd doping, electrical charachteristics, conduction mechanism

Abstract

Pure single phase $BiFeO_3$ and Gd doped $BiFeO_3$ with different Gd doping levels were synthesized through a metalorganic route. Quasi-epitaxial (columnar) $BiFeO_3$ films were fabricated on the top of $SrTiO_3$ substrates with preferred orientation. The rectifying properties of Nb:$SrTiO_3$-$BiFeO_3$-Pt structures, in which the $BiFeO_3$ layer was doped with

Gd (0 %; 5 %; and 10 %), were investigated by measuring current-voltage characteristic at different temperatures. It was found that the structures show a diode-like behavior with reverse bias for negative polarity and forward bias for positive polarity applied on the top Pt contact. The potential barrier was estimated for negative polarity assuming a Shottky-like thermionic emission with injection controlled by the interface and the drift controlled by the bulk. It was found that the height of the potential barrier is dependent on the Gd doping, being 0.32 eV for zero doping, 0.45 eV for 5 % doping and 0.60 eV for 10 % doping. The result is explained by the partial compensation of the p-type conduction induced by Bi volatility with Gd doping. The Fermi level moves upward as the doping concentration increases leading to a higher potential barrier for holes.

BIZMUT FERRIT İNCE FILMLERIN SENTEZI VE ELEKTRKSEL KARAKTERIZASYONU

Hamidreza Khassaf

Malzeme Bilimi ve Mühendisliği, Yüksek Lisans Tezi, 2012

Tez Danışmanı: Yrd. Doç. İ. Burç Mısırlıoğlu

Keywords:

Özet

Saf ve farklı oranlarda Gd katkılı $BiFeO_3$ sentezi metalorganik bir metot ile gerçekleştirilmiştir. Yarı-epitaksiyel (kolonsal) $BiFeO_3$ filmler $SrTiO_3$ altlıklar üzerinde büyütülmüştür. %5 ve %10 Gd katkılı $BiFeO_3$ tabakasına sahip Nb:$SrTiO_3$-$BiFeO_3$-Pt yapısının iletim özellikleri akım-voltaj ölçümleri ile farklı sıcaklıklarda belirlenmiştir. Numunelerin Pt üzerinde negative voltajda ve pozitif voltajdaki akım davranışından bir diyot gibi davrandıkları ortaya konmuştur. Eşik enerjisi negative voltajda arayüzeydeki yük girişi Schottky benzeri termoiyonik emisyon ile belirlenen ve takip eden sürüklenme davranışı da iç kısımlar tarafından control edilen bir mekanizma düşünülerek bulunmuştur. Arayüzeydeki eşik enerjisinin Gd katkısına bağlı olduğu tespit edilmiştir ve katkısız filmler için bu değer 0.32 eV, 5% katkı için 0.45 eV ve 10% katkı için de 0.60 eV olarak hesaplanmıştır. Gözlemlenen davranış Bi boşluklarına bağlı meydana gelen p-tipi iletkenliğin Gd katkısı ile kompanse edilmesi şeklinde açıklanmıştır. Katkı miktarı arttıkça Fermi seviyesi de yukarı doğru çıkmakta ve electron boşlukları için eşik enerjisini yükseltmektedir.

ACKNOWLEDGEMENTS

First and foremost, I would like to thank my supervisor Dr. Burç Mısırlıoğlu for his support, patience and steadfast encouragement to complete this work.

Dr. Lucian Pintilie, director of the National Institute of Materials Physics, Magurelle-Romania who spent a lot of time guiding me in spite of his busy schedule and my co-advisors Dr. Ebru Alkoy and Dr. Sedat Alkoy, who helped me to carry out this work.

I would also like to thank my reading committee members, Dr. Cleva Ow-Yang, Dr. Mehmet Ali Gülgün, Dr. Gözde İnce, Dr. Ali Koşar and Dr. Mehmet Yıldız for the helpful comments on the draft of this thesis.

I acknowledge the funding provided by TUBITAK and also the support provided by the Turkish Academy of Sciences-GEBIP program. I am grateful of the administration of the National Institute of Materials Physics, Magurelle-Romania that made it possible to use their equipment.

TABLE OF CONTENTS

List of Tables ix

List of Figures x

Chapter 1 INTRODUCTION: FERROELECTRICITY 1

1.1 Definition and Properties 1

1.2 Cubic Perovskite Structure 1

1.3 Hysteresis Loop 2

1.4 Hysteresis Loops and Microstructure 5

1.5 Domain Formation 6

1.6 $BiFeO_3$ Perovskite Structure 7

Chapter 2 BISMUTH FERRITE SYNTHESIS AND THIN FILM FABRICATION 11

2.1 $BiFeO_3$ Synthesis 11

2.2 Growth and Characterization of Pure and Doped $BiFeO_3$ Thin Films 17

2.3 $BiFeO_3$ Thin Film Fabrication 20

2.4 Electrical Characterization 22

2.5 Metal-ferroelectric-metal Structures 22

2.6 Schottky contact 24

2.7 Ohmic contact 27

2.8 Conduction Mechanisms in Ferroelectrics 27

2.9 Ferroelectric $BiFeO_3$ Thin Film Capacitor and Its Electrical Properties 29

Chapter 3 CONCLUDING REMARKS AND FUTURE WORK 51

3.1 Conclusion 51

3.2 Future Work 52

Bibliography 53

List of Tables

Table 1: The estimated values for the density of free carriers n and for the built-in potential V_{bi} for different values of the Gd doping. The estimates were performed considering a thickness of about 200nm for the $BiFeO_3$ films and a value of 800 for the static dielectric constant. The last value is based on the fact that the capacitance value at -1V is about the same for all samples.. 49

List of Figures

Figure 1.1: Perovskite structure. A atoms are situated at each corner of the cube, smaller B atom sits at the body center and 6 of O atoms share 6 face centers of the cube. 2

Figure 1.2: Alignment of dipole domains in ferroelectric phase. a) Antiparallel alignment, namely domains before application of any electric field. b) Growing of domains inexistence of the electric field in the same direction. c) Application of higher electric field: All crystal polarized parallel to the field. d) Dipoles forming the “remnant polarization” state in spite of removal of the field 3

Figure 1.3: Schematic depicting the alignment of dipoles in paraelectric phase. There is no alignment with any application of electric field in the beginning. The middle picture shows the growing of “up” alignment in existence of the electric field. The bottom picture exhibits the relaxation of “up” aligned dipoles with removal of electric field. 4

Figure 1.4: Hysteresis loops of a) ferroelectric with spontaneous and remnant polarization and b) paraelectric phase ($T>T_C$) with linear relation between polarization and external field. 4

Figure 1.5: The hysteresis loops of an epitaxial PZT film (left) and a polycrystalline PZT film. Compositions and thicknesses of the films are the same. Black loops recorded in the dynamic mode and red ones are hysteresis loops recorded in the static mode [4].. 5

Figure 1.6: A free standing ferroelectric, surface is exposed to air, domain splitting due to depolarizing field b) Total compensation of bound charges by ideal electrode charges c) Partial compensation of bound charges by non-ideal electrode charges, a finite screening length at the metal surface.. 7

Figure 1.7: Perovskite structure of $BiFeO_3$.. 9

Figure 1.8: Displacement of iron atoms forming of permanent dipoles........................... 10

Figure 2.1: Flowchart of the synthesis process for obtaining pure $BiFeO_3$ phase............ 12

Figure 2.2: Calcination path for synthesis of bismuth ferrite both in bulk and film form 13

Figure 2.3: XRD patterns of $Bi_{(1-x)}Gd_{(x)}FeO_3$ powders 14
Figure 2.4: A typical SEM image of the synthesized $BiFeO_3$. Grain size is about 300 nm and the structure is more or less uniform. 15
Figure 2.5: DTA curves for various Gd doping levels of $BiFeO_3$ powder. The upper curve in each plot represents the data collected during cooling and a downward peak represents phase change as an exothermic formation. 10% Gd doped sample has no apparent transition. 16
Figure 2.6: XRD peaks of $BiFeO_3$ before and after exerting DTA temperature regime. There is no extra phase formation meaning TG/DTA analyze can be trusted to be for pure $BiFeO_3$ phase. 17
Figure 2.7: The XRD pattern of the fabricated $BiFeO_3$ film. The structure is an epitaxy imposed by $SrTiO_3$ substrate. 21
Figure 2.8: The SEM image of $BiFeO_3$ film. There is preferred orientation imposed by the (100) $SrTiO_3$ substrates. 21
Figure 2.9: The band diagram for a metal-ferroelectric-metal structure. *B.C.* is conduction band; *B.V.* is valance band, V'_{bi} the built-in voltage in the absence of the ferroelectric polarization; V'_{bi} is the built-in voltage with polarization; Φ_B^0 is the potential barrier in the absence of the ferroelectric polarization (The figure is made for a p-type ferroelectric but the discussion is also valid for an n-type material.). 24
Figure 2.1: Current voltage characteristics of a single phase $BiFeO_3$ sample in different temperatures 29
Schottky representation at constant voltage is: 30
Figure 2.11: Schottky representation at constant voltage 30
Figure 2.12: Examples of Schottky emission at constant tmperature 31
Figure 2.13: Temperature independency in *F(T)* versus *100/T* 32
Figure 2.14: Arrhenius representations at constant voltage 32
Figure 2.15: Activation energy versus $V^{1/2}$ 33
Figure 2.16: The log-log representation for the I-V characteristics of $BiFeO_3$ sample at 300K 33
Figure 2.17: Current voltage characteristics of a 5% Gd doped $BiFeO_3$ sample in different temperatures 34

Figure 2.18: *$ln(I/T^{3/2})$~1000/T* representation 35
Figure 2.19: apparent potential barrier as function of $V^{1/4}$ 36
Figure 2.20: Current voltage characteristics of a 10% Gd doped $BiFeO_3$ sample in different temperatures 36
Figure 2.21: *$ln(I/T^{3/2})$~1000/T* representation 37
Figure 2.22: apparent potential barrier as function of $V^{1/4}$ 37
Figure 2.23: $1/C^2$ versus V diagram in 5% Gd doped $BiFeO_3$ 38
Figure 2.24: $1/C^2$ versus V diagram in 10% Gd doped $BiFeO_3$ 39
Figure 2.25: (a) XRD pattern of the pure $BiFeO_3$ film where 1 and 2 denote (100) and (200) peaks of the film, respectively. Note that Gd doped films have nearly the same pattern (not shown here), (b) C-V characteristics at room temperature for single phase $BiFeO_3$ layer. Measurement performed at 100kHz with amplitude of 0.1V for ac signal. 41
Figure 2.26: I-V characteristics at room temperature for different Gd doping of the $BiFeO_3$ layer 42
Figure 2.27: I-V characteristics at different temperatures for $BiFeO_3$ films with no Gd doping (a), with 5 % Gd doping (b) and with 10 % Gd doping (c). 43
Figure 2.28: The voltage dependence of the potential barrier in the case of $BiFeO_3$ films with different Gd doping, on $SrTiO_3$:Nb substrates. The confidence factor for the linear fit is in all cases higher than 0.99 47
Figure 2.29: The $1/C^2$ representation for the pure $BiFeO_3$ film. 49

LIST OF SYMBOLS AND ABBREVIATIONS

FE	:	ferroelectric
E_i	:	electric field components
D_i	:	dielectric displacement components
E	:	energy level
T_C	:	Curie temperature
F	:	free energy
STO	:	Strontium Titanate
RT	:	Room temperature, 25 °C
Φ	:	work function
δ	:	potential
π	:	charge density
χ_0	:	permittivity of vacuum
χ_i	:	relative permittivity

Chapter 1 INTRODUCTION: FERROELECTRICITY

1.1 Definition and Properties

Ferroelectricity is a property of a certain class of materials, which possess a spontaneous electric polarization due to the presence of electric dipoles at the unit cells because of asymmetrical atomic shift or arrangements in the unit cell below a critical temperature. This asymmetry gives rise to a permanent dipole moment in the cell that that can be manipulated by the application of an external electric field [1]. Ferroelectric behavior is defined to be the result of a structure transition, giving rise to dipoles in the unit cell.

1.2 Cubic Perovskite Structure

There are materials with different crystal structures showing ferroelectric behavior but one of the most well-known crystal structures in which the ferroelectricity occurs is the cubic perovskite structure. The general formula of the cubic perovskite is often ABO_3 oxide and it forms in a cubic or pseudocubic structure. In perovskite structure, A (monovalent or divalent metal) and B (tetravalent or pentavalent metal) locations attain valence capacities in the range of 2+ and 4+ and O is the O^{2-} anion [2]. Covalencies must also be considered in this structure, leading to corrections in the charges of these ions as effective values. A atoms are situated at each corner of the cube, smaller B atom sits at the body center and 6 of O atoms share 6 face centers of the cube, coordinating an octahedra around atom B [3]. Figure 1.1 is the prototype shape of the perovskite, and behaves as a paraelectric phase.

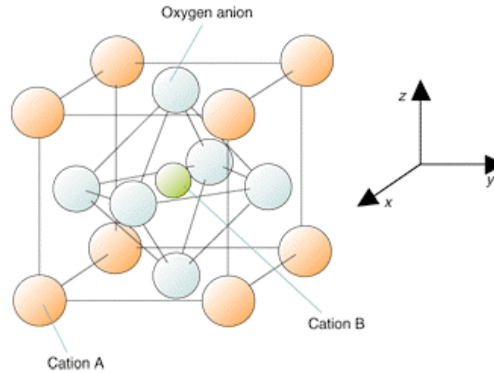

Figure 1.1: Perovskite structure. A atoms are situated at each corner of the cube, smaller B atom sits at the body center and 6 of O atoms share 6 face centers of the cube.

The ferroelectric phase transition occurs at a critical temperature called the Curie point (TC). Above the Curie temperature, the crystal is a centrosymmetric paraelectric (cubic geometry, and a high symmetry with respect to the central B-site). Below the Curie temperature the crystal is no longer centrosymmetric and will form off-centre structural distortions, which result in ferroelectric behavior [2]. In this situation at least one symmetry operation (or element) that was possible in one of the phases is lost. $BaTiO_3$ and $PbTiO_3$ are two examples for perovskite structure materials with such ferroelectric transition. $BaTiO_3$ and $PbTiO_3$, transform from cubic to tetragonal at 130°C and 493°C, respectively accompanied by the appearance of a spontaneous dipole in their unit cells [3].

1.3 Hysteresis Loop

In ferroelectrics, parameters such as temperature, stress, geometry and type of material can affect the magnitude as well as the direction of spontaneous polarization. Spontaneity of polarization disappears above the Curie point and the ferroelectric transforms into a paraelectric. Assuming there is no external electric field bellow the Curie point, Figure 1.2 shows a schematic of microscopic crystal domain orientation of a ferroelectric phase. Before applying electric field, the microstructure will exist in a state where anti-parallel oriented polarized domains (clusters of parallel aligned dipoles) are present. In this

situation there is electrostatic neutrality meaning their total polarization sums to zero. Such a state is energetically more favorable compared to a single domain state. Whether a single domain or multidomain state exists strongly depend on whether or not the system has electrodes. In the rest of the study, electrodes will be assumed to be compensating the bound charges at the ferroelectric surface at the ferroelectric surface due to the presence of spontaneous dipoles.

The domains of anti-parallel polarization start to align parallel to the field when the electric field starts to be applied and that creates a total nonzero polarization inside the crystal. As the electric field is increased, more anti-parallel domains align parallel to the field. Polarization saturation occurs eventually when the whole crystal is polarized in the same direction to its maximum (P_S). After saturation; unlike paraelectrics (See Figure 1.3), the parallel dipoles do not relax back to their original anti-parallel states with the removal of external field: They can remain in an all parallel configuration for some indefinite amount of time in the presence of free surfaces (See Figure 1.2). As, for some time, they prefer to be in the polarized state at zero electric field (Remnant polarization, P_R) and a negative field (coercive field, E_C) is required to switch the total polarization in the reverse direction. Therefore, as it can be seen in Figure 1.4, ferroelectrics behave similar to ferromagnetics in the sense of hysteretic behavior.

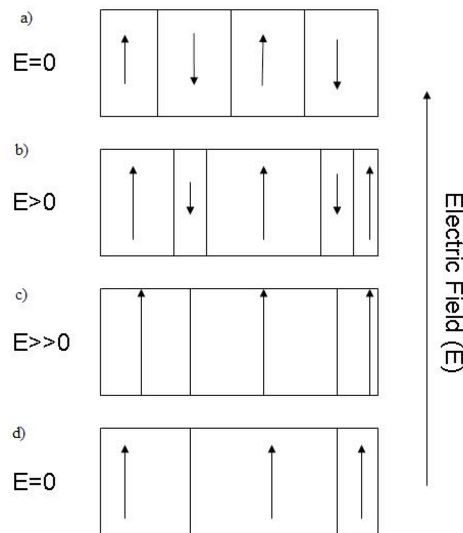

Figure 1.2: Alignment of dipole domains in ferroelectric phase. a) Antiparallel alignment, namely domains before application of any electric field. b) Growing of domains in

existence of the electric field in the same direction. c) Application of higher electric field: All crystal polarized parallel to the field. d) Dipoles forming the “remnant polarization” state in spite of removal of the field.

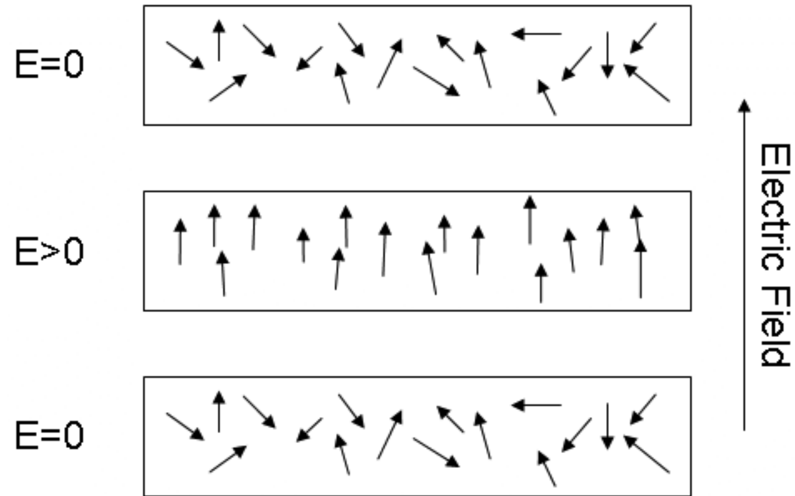

Figure 1.3: Schematic depicting the alignment of dipoles in paraelectric phase. There is no alignment with any application of electric field in the beginning. The middle picture shows the growing of “up” alignment in existence of the electric field. The bottom picture exhibits the relaxation of “up” aligned dipoles with removal of electric field.

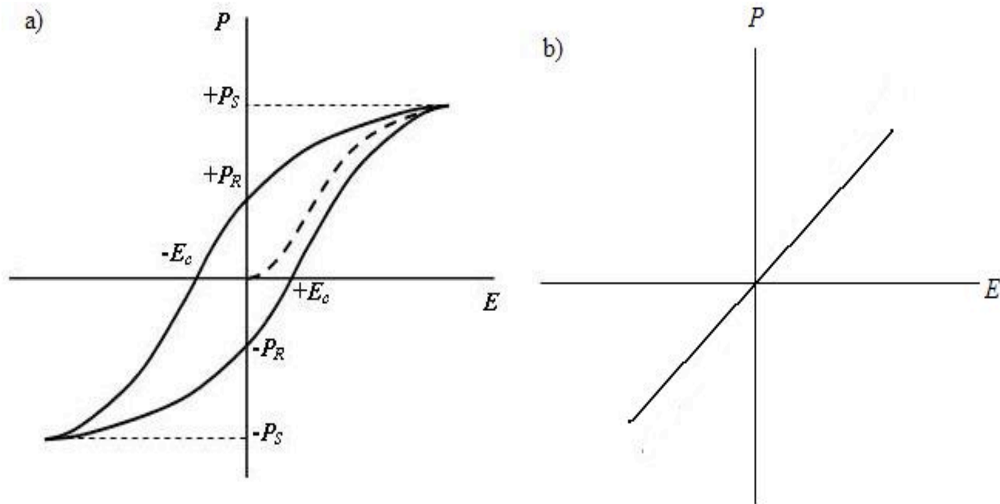

Figure 1.4: Hysteresis loops of a) ferroelectric with spontaneous and remnant polarization and b) paraelectric phase ($T>T_C$) with linear relation between polarization and external field.

1.4 Hysteresis Loops and Microstructure

Experimental data show that the hysteresis behavior is strongly dependent on the type of crystal orientation. Figure 1.5 is the hysteresis loops of two PZT samples with same composition and different crystal orientation (polycrystalline and epitaxial).

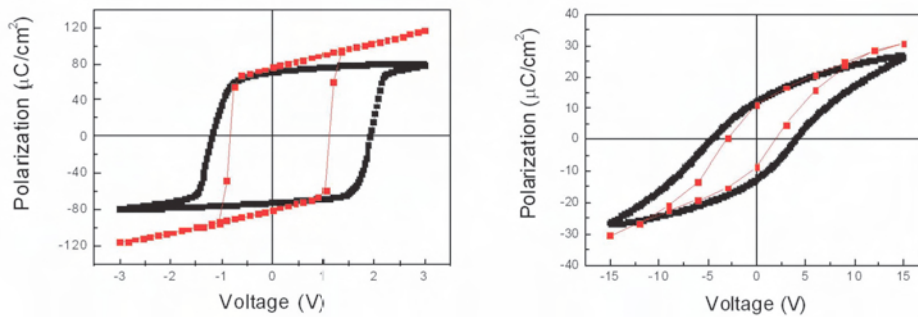

Figure 1.5: The hysteresis loops of an epitaxial PZT film (left) and a polycrystalline PZT film. Compositions and thicknesses of the films are the same. Black loops recorded in the dynamic mode and red ones are hysteresis loops recorded in the static mode [4].

In the case of epitaxial film, an almost rectangular loop forms while in the polycrystalline film the loop is elongated along the voltage axis. On the other hand, polycrystalline structures have slower response time to any change in polarization state. This is attributed to two main reasons: presence of grain boundaries, which will lead to high resistivity and high dielectric constant. Coercive voltage is another factor that is making difference between the two structures. It will be smaller in epitaxial films, which suggests that the absence of grain boundaries is beneficial for polarization switching since they are natural obstacles for the movement of domains.

1.5 Domain Formation

There will be a formation of an electric field in the surface of ferroelectric after the formation of spontaneous polarization. Presence of this surface electric field is attributed to the bound charges, populated on the surface. This electric field is called “depolarizing field” due to its opposite orientation to the spontaneous polarization.

Whenever there is a non-homogeneous distribution of spontaneous polarization, there will be a formation of the depolarizing field due to the fall-off of the polarization near the free surface of a ferroelectric (polarization is zero outside the ferroelectric and nonzero inside) [5].

If the depolarizing field is strong enough, it can cause break down of the single domain state. In that situation, there will be domain formation with micron-sized clusters of dioples in opposite orientations so that the electrostatic energy becomes minimized [6]. Another possibility regarding the minimization problem of the depolarizing field is the contribution of free charges from a surrounding material, like an ideal metal electrode to compensate the depolarizing field. Taking this to account that electrodes always deviate from ideal behavior and most of the times don’t completely compensate for depolarizing field, ferroelectric domains with domain widths form depending on the competing strengths of depolarizing field and spontaneous polarization. Figure 1.6 is a schematic of domain formation in ferroelectrics.

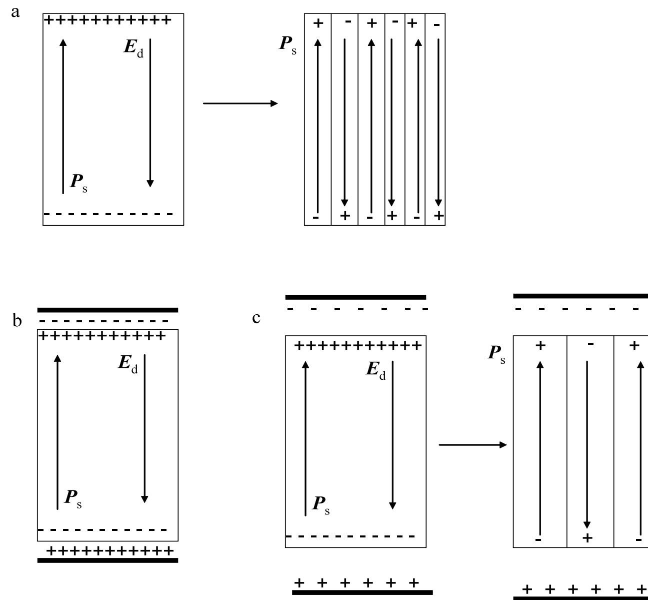

Figure 1.6: A free standing ferroelectric, surface is exposed to air, domain splitting due to depolarizing field b) Total compensation of bound charges by ideal electrode charges c) Partial compensation of bound charges by non-ideal electrode charges, a finite screening length at the metal surface.

Ferroelectric domains undergo three different steps during a P-E test:

- Initial formation of the ferroelectric domains in the opposite direction of polarization (nucleation)
- Growth of the ferroelectric domains with polarization parallel to the applied electric field [7,8,9]
- Compensation of the depolarization field occurring just after the switching is taking place [10]

1.6 $BiFeO_3$ Perovskite Structure

An example of perovskite structures is bismuth ferrite ($BiFeO_3$) that attracts attention not only because of its ferroelectric properties but also because of its magnetic ordering

coupled with its ferroelectric behavior. The idea of using multiferroics[1] in applications for multifunctional device components arouses interest on materials in which the magneto-electric property is tailored. In these materials polarization and magnetization can be weakly or strongly coupled [11]. It should be noted a certain class of materials, prominently oxides exhibit the presence of a magnetic structure along with ferroelectricity in the same phase [12].

The fact that $BiFeO_3$ (BFO) is a compound showing ferroelectromagnetic behavior and has uniquely high temperatures of magnetic and electric ordering, has made it a very prospective and probably the most widely studied material for the applications in non-volatile ferroelectric random access memory (NVFRAM), dynamic random access memory, sensors and micro-actuators [13].

$BiFeO_3$ in bulk form exhibits spontaneous polarization (Ps) along the (111) direction. This could shift to other directions such as (100) upon growth on a misfitting substrate as a result of elastic coupling. Very high Ps values have been reported for $BiFeO_3$ films on single crystal substrates making these systems attractive for memory and high-k layers. However, a serious problem of $BiFeO_3$ that has greatly limited its applications is that it has very high values of leakage current. This high amount of leakage current is mainly attributed to deviation from oxygen stoichiometry and high defects density [14].

The perovskite $BiFeO_3$ was firstly produced in the late 1950s and like today, many of the early studies were focused on its potential for magnetoelectric coupling. However, unlike today's most efforts on working on the preferred orientations grown $BiFeO_3$, the early work on bismuth ferrite was mainly focused on the bulk form. In the early 1960s $BiFeO_3$ was suspected to be an antiferromagnetic, ferroelectric multiferroic [15].

$BiFeO_3$ shows simultaneous coexistence of ferroelectric and antiferromagnetic behavior and it has a high phase transition temperatures (Curie temperature of 1083K, and Néel

[1] Materials exhibiting simultaneous ferroelectric and ferromagnetic properties are known as multiferroics (magneto-electrics). The idea of using multiferroics in applications including data storage arouses interest to work on materials that are expected to show multiferroic behavior theoretically. However there are a lot of bottlenecks researchers should deal with in order to make a phase show admissible multiferroic behavior in practice.

temperature of 657K) [16], which means that $BiFeO_3$ is a stable ferroelectric in room temperature showing magnetic behavior in the meantime.

$BiFeO_3$ exhibits spontaneous polarization along the [100] direction. However, a serious problem with $BiFeO_3$ that has greatly limited its applications is that it has very high values of leakage current. This high amount of leakage current is mainly attributed to deviation from oxygen stoichiometry and high defects density [17]. There are charge defects present in the system such as bismuth vacancies (V_{Bi}) and oxygen vacancies (V_O). Creation of V_O is a result of Bi volatility and the transition from Fe^{3+} to Fe^{2+}. (1.1 suggests that charged defects governed by Fe^{2+} ions, oxygen vacancies V_O and/or bismuth vacancies V_{Bi} may appear in both the deoxygenated $BiFeO_3$ phases and deoxygenated impurity phases. These V_O and/or V_{Bi} vacancies will reduce the electrical resistivity of the samples, giving rise to high leakage currents in the samples [18]. In this situation, theoretical prediction of observing multiferroic behavior turns into high conductivity due to valence fluctuation between Fe3+ and Fe2+ ions and oxygen deficiency in the system.

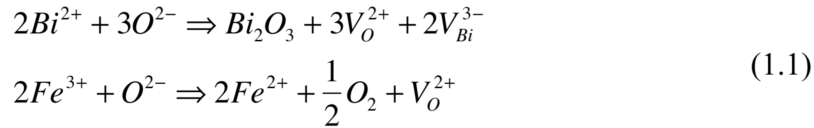

$$\begin{aligned} &2Bi^{2+} + 3O^{2-} \Rightarrow Bi_2O_3 + 3V_O^{2+} + 2V_{Bi}^{3-} \\ &2Fe^{3+} + O^{2-} \Rightarrow 2Fe^{2+} + \frac{1}{2}O_2 + V_O^{2+} \end{aligned} \quad (1.1)$$

In the case of bismuth ferrite, the crystal structure is a rhombohedrally slightly distorted simple perovskite. Positions of Bi, O and Fe in $BiFeO_3$ structure are shown in Figure 1.7.

Below the Curie temperature, the cubic lattice will be tetragonally distorted (Figure 1.8), which is a displacive ferroelectric phase transition. As mentioned before, bismuth ferrite exhibits a rhombohedral ferroelectric phase [2].

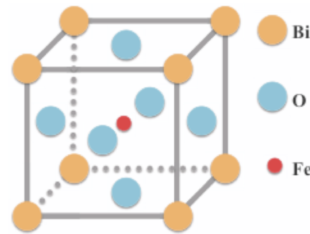

Figure 1.7: Perovskite structure of $BiFeO_3$

As in Figure 1.8 Local atomic arrangement in perovskite structure can acquire a position so that there will be some remnant polarization after applying sufficient electric field. In this situation unit cells contain a permanent electric dipole.

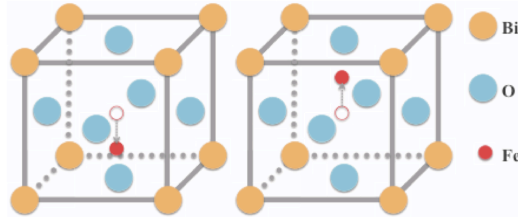

Figure 1.8: Displacement of iron atoms forming of permanent dipoles

Variety of atoms occupying A-site and B-site positions in oxide perovskites create different mechanisms of ferroelectricity and various levels of magnetic substructure. In $BaTiO_3$ for instance, ferroelectricity is attributed to the centered Ti while the lone-pair Pb ion is dominant in $PbTiO_3$ [19]. In our study case $BiFeO_3$ the later one is the case where the polarization is mostly caused by the lone pair of Bi^{3+}, meaning the A-site positions involvement while the magnetization comes from the B-site (Fe^{3+}) [20]

Chapter 2 BISMUTH FERRITE SYNTHESIS AND THIN FILM FABRICATION

2.1 $BiFeO_3$ Synthesis

In order to synthesis the $BiFeO_3$, several techniques have been used to overcome its leakage problem. Solid-state reaction [21], co-precipitation method [22] and soft chemical route [12] are some methods that have been used to synthesis $BiFeO_3$ with minimum leakage current. On the other hand, it is crucial to introduce a well-defined fabrication procedure of synthesizing pure single phase $BiFeO_3$. A slight change in procedure parameters could lead to forming other impurity phases present in Bi-Fe-O system, such as $Bi_2Fe_4O_9$, $Bi_2O_{2.75}$, $Bi_{36}Fe_{24}O_{57}$ and $Bi_{46}Fe_2O_{72}$ [23,24].

In our work, we used chemical solution deposition method to obtain $BiFeO_3$ single phase and investigate electrical properties of $BiFeO_3$ with and without presence of doping elements such as La and Gd in the film form. Flowchart given in Figure 2.1 is an outline of the sol-gel method we used for the synthesis procedure. Bismuth nitrate pentahydrate [$Bi(NO_3)_3.5H_2O$] and iron nitrate nonahydrate [$Fe(NO_3)_3.9H_2O$] (99.99% Sigma-Aldrich) were used as Bi and Fe based chemicals respectively. By dissolving Bi and Fe nitrates in ethylene glycol and acetic acid separately followed by mixing at room temperature, we obtained a transparent precursor solution. This precursor solution was used both in powder synthesis and in spin coating to fabricate near-epitaxial films. It should be mentioned here that by epitaxy we mean strongly textured grown films toward preferred direction (here [100] direction). TEM characterization will be necessary to comment on the structural properties of the grown films in term of single crystal growth. In our case we assume that the film is forming in the separate islands (nucleation) and then grows to form a uniform structure.

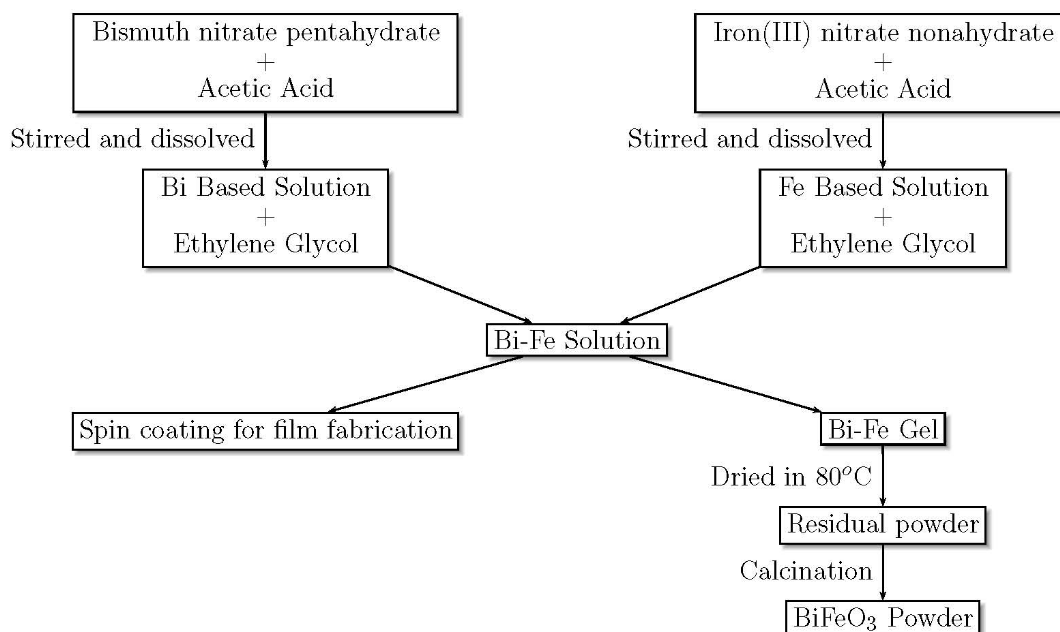

Figure 2.1: Flowchart of the synthesis process for obtaining pure $BiFeO_3$ phase

Drying the same precursor solution in 80°C for about two days gave us a residue-gel ready for calcination stage after grinding in agate. In order to compensate the evaporation loss of Bi (causing due to the volatility of bismuth) during post-annealing process, excess Bi utilized. Thermo-gravimetric and differential thermal analysis (Netzsch, STA 449C) were performed in N_2 atmosphere from 25°C to 900°C at a heating rate of 10°C/min to determine the transition temperature of pure and doped powders. The structure of the powders calcined at various doping levels was characterized by an X-ray diffractometer (BRUKER axs XRD) with Cu K radiation.

To investigate the effect of A-site doping, Gd, La and Sm elements were added in different doping levels (5, 10 and 15%). For Gd doping, gadolinium nitrate hexahydrate [$Gd(NO_3)_3.6H_2O$], for La, lanthanum nitrate hexahydrate [$La(NO_3)_3.6H_2O$] and for Sm, samarium nitrate hexahydratewere [$Sm(NO_3)_3.6H_2O$] all 99.99% from GFS chemicals substituted to same percentage of bismuth nitrate pentahydrate in the first stage.

A two-stage thermal path was used for calcination where the precursor solutions were kept in 550°C and 700°C each for 1 hour and the heating rate was 10°C/min. Then powders were free-cooled down to room temperature to get $BiFeO_3$ phase (Figure 2.2).

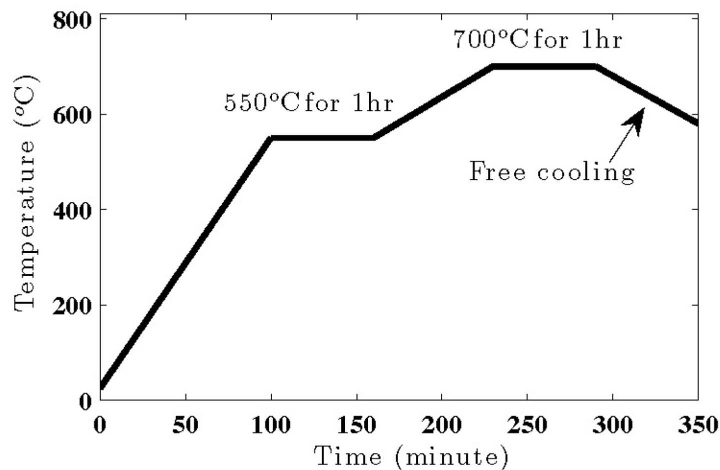

Figure 2.2: Calcination path for synthesis of bismuth ferrite both in bulk and film form

In previous studies on $BiFeO_3$, the purity of the phase is mostly reported to be related to the temperature, atmosphere and time at the calcination stage [23,25,26] as well as the type and amount of doping elements [12]. Our findings suggest that a combination of drying stage and calcination path is the most important part of the synthesis. It is crucially important to dry the solution in a particular temperature to prevent obtaining precocious gel. In Gd doping for instance, single phase $BiFeO_3$ can form in different heat treatment paths during calcination for different Gd doping levels when the drying stage is done properly as long as the gel is not precocious. We noted that doping with Gd more than 10% could lead to secondary phase formation. Figure 2.3 perovides a comparison between XRD patterns of $Bi_{(1-x)}Gd_{(x)}FeO_3$ (x=0.01, 0.05, 0.07 and 0.1).

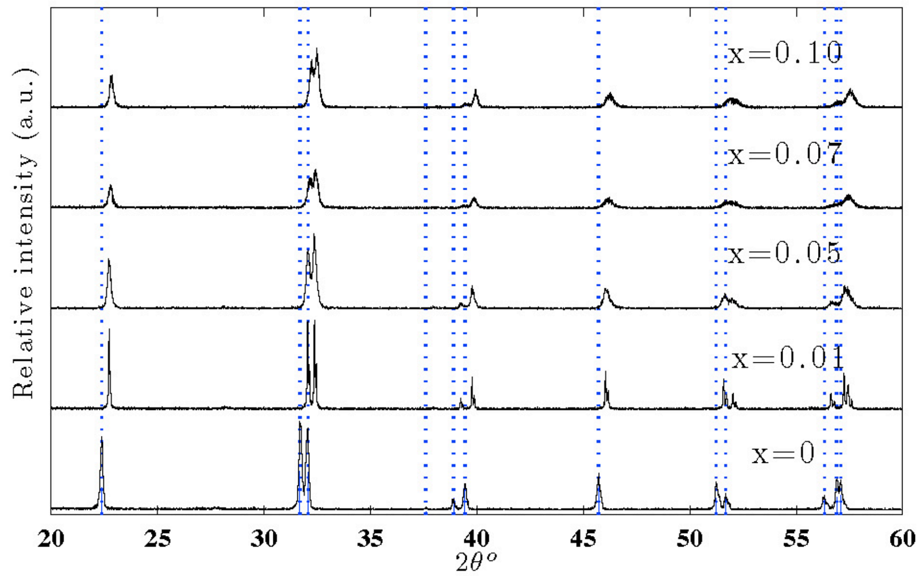

Figure 2.3: XRD patterns of $Bi_{(1-x)}Gd_{(x)}FeO_3$ powders

With increasing Gd content, there is a noticeable peak shift towards higher Bragg angles with respect to the pure $BiFeO_3$ peaks and this is an indication of shrinkage in the lattice parameters of the cubic perovskite. As Gd has a slightly smaller ionic radius than Bi, this outcome can naturally be explained. The obtained phase is a uniform powder with almost no porosity in the structure. However, doping makes visible change in the grain size, which needs further studies to see how doping has impact on growth and physical characteristics if the phase. Figure 2.4 exhibits the microstructure of typical synthesized $BiFeO_3$ by using the described method.

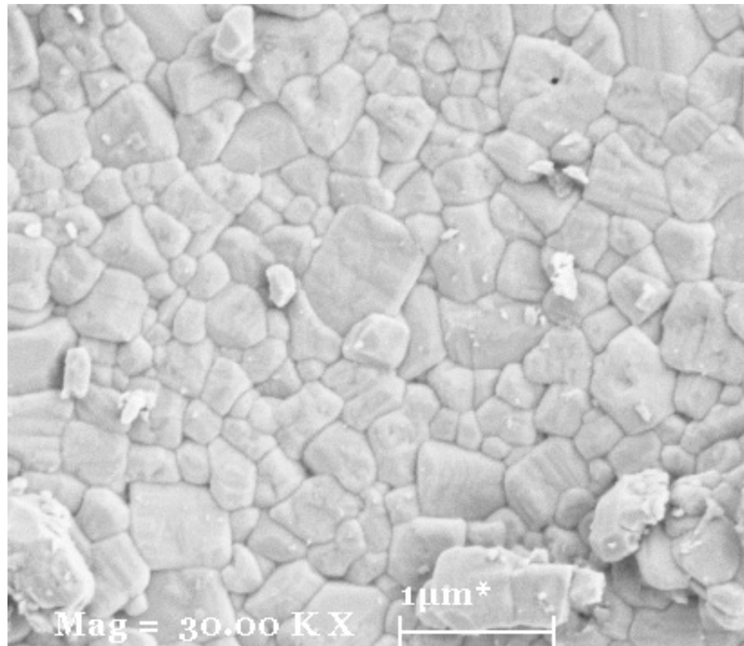

Figure 2.4: A typical SEM image of the synthesized $BiFeO_3$. Grain size is around 300 nm and the structure is more or less uniform.

What is important here is that such a reduction in lattice parameters with increasing Gd content should be expected to impact the T_C, which we find worthy to investigate. To do so we carried out TG/DTA experiments. Our results show that Gd doping decreases T_C dramatically (See Figure 2.5) in such a way that after increasing doping level to 10% T_C will disappear.

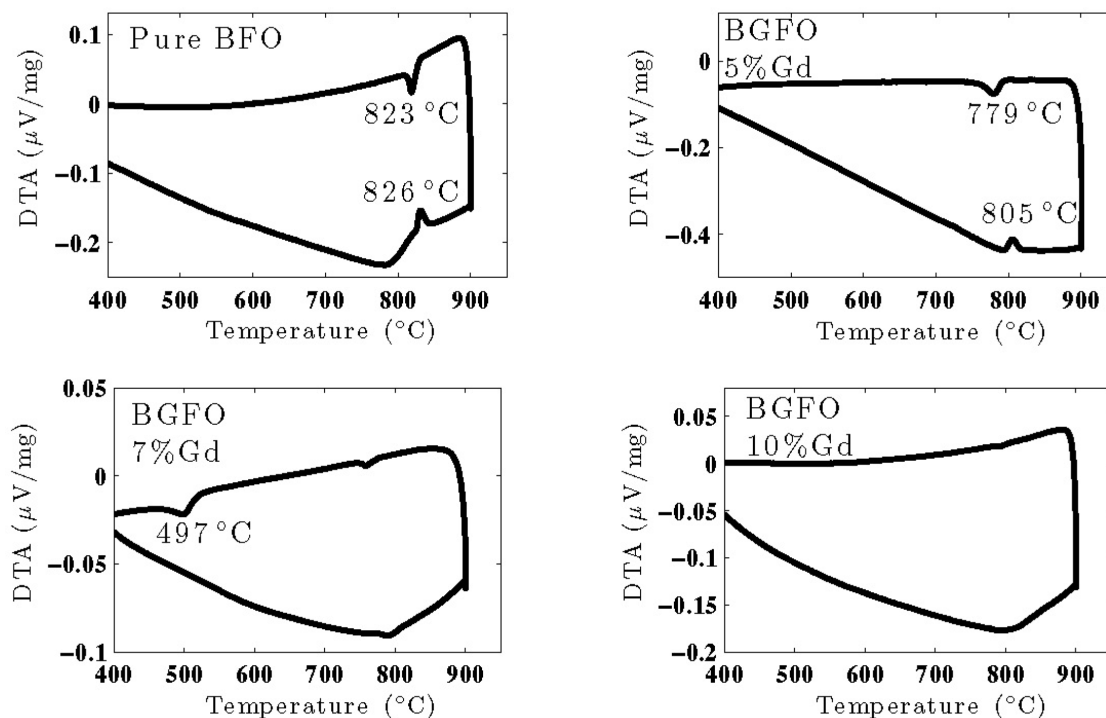

Figure 2.5: DTA curves for various Gd doping levels of $BiFeO_3$ powder. The upper curve in each plot represents the data collected during cooling and a downward peak represents phase change as an exothermic formation. 10% Gd doped sample has no apparent transition.

To make sure that the temperature at the value of 900°C will not effect the synthesized $BiFeO_3$ in terms of forming new phases that might change DTA results, the stability of the obtained $BiFeO_3$ was checked at high temperatures. To do so, crystallized $BiFeO_3$ powder was heated up with the same regime exerted in the TG/DTA to the samples. The structure of the sample was checked after this heat treatment through XRD analysis. XRD results confirm that there is no extra chemical phase formation during the DTA/TG test (See Figure 2.6.).

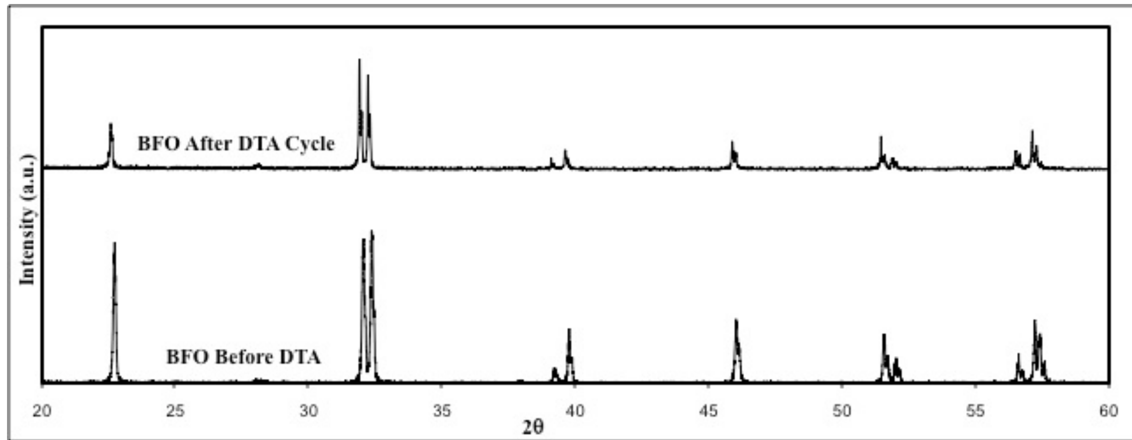

Figure 2.6: XRD peaks of $BiFeO_3$ before and after exerting DTA temperature regime. There is no extra phase formation meaning TG/DTA analysis can be trusted to be pure $BiFeO_3$ phase.

2.2 Growth and Characterization of Pure and Doped $BiFeO_3$ Thin Films

A thin film is a layer of material ranging from fractions of a nanometer (monolayer) to several micrometers in thickness. The miniature dimensions in thin films takes into account several inferior electrical properties when thin film is being compared with bulk materials. For instance, if in the case of bulk ferroelectrics, especially in the form of ceramics, the leakage can usually be negligible, in the case of the thin films the leakage currents can be large enough to hide any contribution from polarization variation [4]. Even small potential drops can produce quite large electric fields in confined volumes such as thin films, triggering certain leakage mechanisms whose details will be perovided in the upcoming sections. Other electrical properties like capacitance, permittivity and remanant polarization can play important role in the electrical characterization of the film. Apart from inferior electrical characterization, there are several exclusive properties like film thickness, type of the substrate, crystal growth orientation, lattice mismatch, concentration of the defects, boundary conditions etc. to investigate. Manipulating each of these parameters could lead to reduction in Curie point and/or intensification of the leakage current in several different ways. For example, the polarization values in a ferroelectric is a strong function of internal strains due to epitaxy on a substrate and the potential barrier at a ferroelectric-electrode interface can significantly be altered by the

value of the polarization or whether multidomain states exist. Therefore it is straightforward to see that the mechanisms for leakage can be quite nonlinearly coupled to the Curie point and the internal strains of a thin ferroelectric film, apart from the chemistry of the interface.

It is obvious that finding a solution to reduce or control the leakage in a metal-ferroelectric-metal structure would be accessible only if the conduction mechanism is correctly understood. It is more crucial to understand the leakage mechanism knowing that leakage has impact on other macroscopic properties. One of the most prominent characteristics of a ferroelectric is the hysteresis observed in the polarization-applied field measurements. For instance, considering that the hysteresis loop in experiments is obtained by the integration of the charge released during the polarization switching, the leakage can have a significant impact on the hysteresis loop. A large leakage current, super-imposed on the switching current will severely alter the hysteresis, masking the presence of ferroelectricity in the analyzed sample. For instance, the magnitude of the average dipole moment density in a ferroelectric can be estimated from the magnitude of switching current at the coercive field in a polarization-electric field hysteresis loop but if leakage currents are more than the switching currents, no such peaks might be observed. Therefore, the study of the charge transport in ferroelectric thin films is of high importance for all the applications using ferroelectric capacitors subjected to an applied external voltage, in order to indentify the conduction mechanisms responsible for the leakage current [27,28,29].

It should be noticed that there are several proposals regarding the origin of the leakage current in ferroelectric thin films: Since the effect of structure quality on the charge transport is not considered so far in studies, several conduction mechanisms could be found for the same material. It means that regardless of the crystal growth of the film, no matter whether it is pure polycrystalline, textured or epitaxial, the ferroelectric thin film capacitor is undergone the application of voltage and current is read when its effect needs to be considered[2] [4]. Furthermore, the fact that any structural defect can impact the

---

[2] A study done by Pintilie et. Al. [32], suggests that crystal orientation makes a significant impact of ferroelectric properties. Capacitance-voltage (C-V) characteristics in the case of two ferroelectric PZT films

density of the free carriers or their mobility is neglected. Having said that the capacitor is consisting of a bulk and interfaces, the electrodes are neglected as well in the studies where they are part of the metal-ferroelectric interface affecting the conduction. So the fit of the experimental data with one or another of the conduction mechanisms is performed without investigating the interface properties and behavior of whatever the metal contact is ohmic or rectifying [30,31].

Traditionally, there is this tendency to come up with a generalized model for different ferroelectric materials, which causes ignoring the subtle structural details. For example, it is accepted that for $PbTiO_3$ and $BaTiO_3$ the origin of the ferroelectricity is the same while the Curie point in $PbTiO_3$ is higher compared to $BaTiO_3$. This is a clue pointing out that the nature of Pb-O and Ba-O bonds are different. The Ba-O bond is nearly an ideal ionic bond, while the Pb-O bond has a high degree of covalency. Thus, sharing the electrons helps to stabilize the spontaneous polarization [32]. Consequently, we should expect different electronic properties for $PbTiO_3$ and $BaTiO_3$ including different mechanisms for the charge transport. It should be kept in mind that ferroelectric polarization makes impact on the charge transport. As explained before, an ideal single domain ferroelectric forms elemental dipoles oriented head-to-tail to give the macroscopic polarization meaning a zero net charge polarization. Thus, all the polarization charges are located near the electrode interfaces, positive on one side and negative on the other. These sheets of bound charges could and must have a certain effect on the interface properties, as for example the barrier height or the width of the depleted region.

Considering the fact that ferroelectrics behave as wide band-gap semiconductors, it would be crucial to understand the contribution of impurities in semiconductor thin films since it is inevitable to have impurities shaping up in the thin film production process. Therefore, general characteristics of metal-semiconductor junctions should be reviewed.

---

with different crystal growth orientation (polycrystalline and epitaxial) but same composition revealed how deep the microstructure can affect the ferroelectric properties. In the case of epitaxial film sharp peaks appeared with switching followed by abrupt changes in the capacitance values once the polarization was reversed. In the polycrystalline films however, the switching produced rounded, broad peaks with no abrupt changes in capacitance value.

2.3 $BiFeO_3$ Thin Film Fabrication

Chemical solution deposition technique is a popular technique being used for depositing thin films. In a typical chemical solution deposition process, a solution containing the constituents of the desired film is applied to a substrate, then dried or heat-treated to drive out the solvent and obtain a solid film. The most common means of applying the solution to the substrate, which we used in our work, is by spin-coating [12,23,25,26,33]. However, there are other methods of depositing the solution such as dip-coating [34], misting, and painting [35] that have been reported to be successful.

The chemical solution deposition method has several considerable advantages over other methods of chemical depositions:

- It takes as short as a couple of minutes to coat several layers on the substrate.
- The film composition is easily changeable layer by layer by varying the solution.
- Using multiple coatings or changing the viscosity of the solution can control the film thickness and uniformity.
- Larger substrates can be coated simply by using more solution in each coating stage [36].

But more importantly, the ease of mixing up a new solution compared to other techniques makes the chemical solution deposition an ideal method for investigations on the effects of doping [37], and film composition [38].

In spin coating, the solution is deposited onto the center of the substrate, which is held by vacuum to a spin chuck. The solution must be taken care of not to contain extra particles (e.g. dust, precipitates) thereby causing test failure. The spin chuck then rotates at a fast rate (in our case 12000 rpm). Centrifugal force uniformly disperses the solution over the entire substrate surface.

After spinning, films are dried further on a hot-plate (in our case at $350^{o}C$ for 5 minutes) or in an oven. This can be followed by spinning on another coat, or by a final annealing process, usually at a higher temperature than the drying step, to obtain a crystalline film [36].

The structure of the obtained films was checked by the XRD to make sure that the fabricated films had epitaxial crystal growth imposed by $SrTiO_3$ substrates (See Figure 2.7).

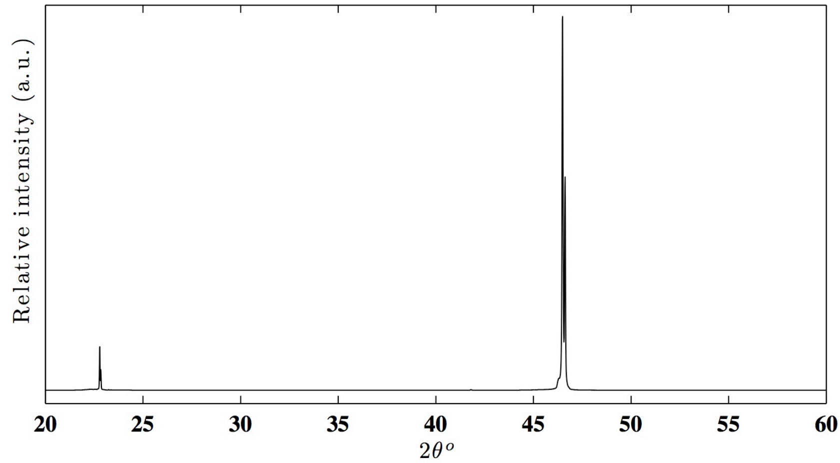

Figure 2.7: The XRD pattern of the fabricated $BiFeO_3$ film. The structure is a semi-epitaxial one imposed by $SrTiO_3$ substrate.

Figure 2.8 presents an SEM image of obtained $BiFeO_3$ film. As it can be seen in this figure, there is preferred orientation for the crystal growth imposed by (100) $SrTiO_3$.

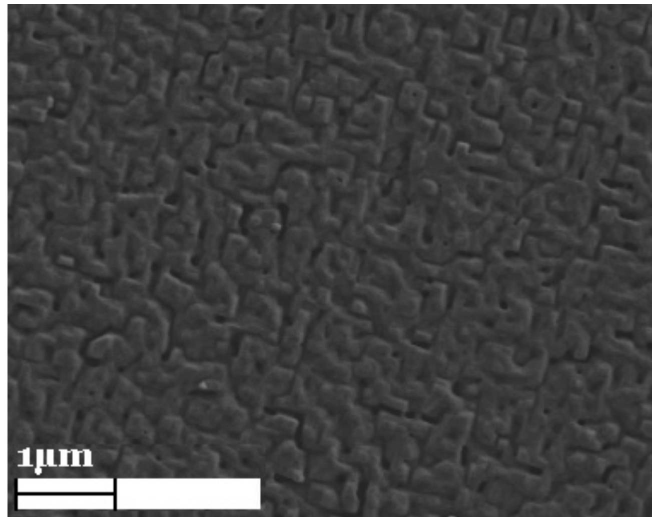

Figure 2.8: The SEM image of $BiFeO_3$ film. There is preferred orientation imposed by the (100) $SrTiO_3$ substrates.

2.4 Electrical Characterization

In order to understand the electrical behavior of the $BiFeO_3$ thin films, we performed variety of electrical characterizations. Firstly, The top Pt contacts of 0.1×0.1 mm^2 were deposited by magnetron RF-sputtering through a shadow mask. The electric measurements were performed at different temperatures in a cryogenic probe station from Lake-Shore (model CPX-VF). The capacitance of the samples were measured with a Hioki LRC bridge, the leakage current with a Keithely 6517 electrometer and the hysteresis loop with a TF2000 ferroelectric tester from AixAcct.

2.5 Metal-ferroelectric-metal Structures

A ferroelectric capacitor is the prototype sample for current-voltage (I-V) measurements. The system consists of two inter-connected sub-systems: the bulk and the electrode interfaces as metal layers (including the possible presence of a depletion region). The two metal layers are deposited on the opposite faces of the bulk layer in such a way that the ferroelectric polarization becomes perpendicular on the metal electrodes. In theory, the electric dipoles shaped up inside the ferroelectric are head-to-tail oriented. Therefore, there will be and end with a sheet of positive charge near one electrode interface and one sheet of negative charge near the other interface. The bulk of the film is free of any net polarization charges because these cancel each other (in an ideal case) except the interfaces with the electrodes.

Taking polarized interfaces into account, it is expected that these charges will affect the quantities specific to classic metal-semiconductor Schottky contacts. A model was developed to take into consideration the effect of polarization charges on the interface properties by Pintilie and Alexe. Following summarized their work in that regard [39]: Specific quantities of a Schottky contact are given in the following equations:

$$V'_{bi} = V_{bi} \pm \frac{P}{\varepsilon_0 \varepsilon_{st}} \delta \tag{2.1}$$

In Equation 2-1, V'_{bi} is the built-in potential where V_{bi} is the built-in potential in the absence of the ferroelectric polarization; P is the ferroelectric polarization; δ is the distance between the polarization sheet of charge and the physical metal-ferroelectric interface; ε_0 is the permittivity of the vacuum; ε_{st} is the static dielectric constant.

$$E_m = \sqrt{\frac{2qN_{eff}(V + V'_{bi})}{\varepsilon_0 \varepsilon_{st}}} \pm \frac{P}{\varepsilon_0 \varepsilon_{st}} \tag{2.2}$$

Where E_m is the maximum field at the interface where q the electron charge; N_{eff} is the effective density of space charge in the depleted region which takes into consideration the ionized donors and capacitors, but also the trapping centers carrying a net charge after capturing a charge carrier.

$$\omega = \sqrt{\frac{2\varepsilon_0 \varepsilon_{st}(V + V'_{bi})}{qN_{eff}}} \tag{2.3}$$

where ω is the width of the depleted region. As it is obvious in the presented equations, all the specific quantities are affected by the presence of the polarization charges. Interestingly, since the polarization charges have opposite signs at the two interfaces the effect is not symmetric. It means that even in a symmetric structure, with identical metal electrodes, presence of the polarization can make the system asymmetrical. Figure 2.9 is a schematic of the band diagram of such a structure. The interface with positive polarization charge imposes an incensement in band bending since the positive charge rejects the holes (positive charges) from the interface region. This will lead to a larger built-in potential compared to the case when the polarization is missing. At the other interface however, the negative polarization charge will attract holes, which will lead to have a smaller band bending.

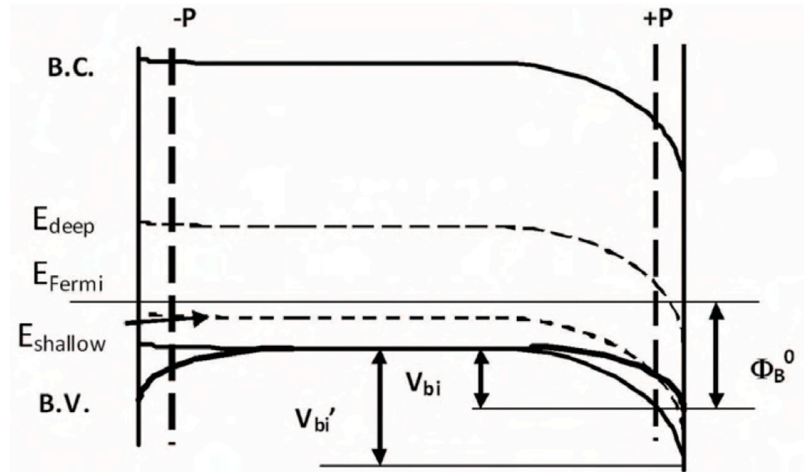

Figure 2.9: The band diagram for a metal-ferroelectric-metal structure. *B.C.* is conduction band; *B.V.* is valance band, V'_{bi} the built-in voltage in the absence of the ferroelectric polarization; V'_{bi} is the built-in voltage with polarization; Φ_B^0 is the potential barrier in the absence of the ferroelectric polarization (The figure is made for a p-type ferroelectric but the discussion is also valid for an n-type material.).

In conclusion, in metal-ferroelectric-metal systems even with identical electrodes in each side, ferroelectric polarization will create an asymmetrical system with different behavior at the interfaces and this will affect all the electrical properties, including the charge transport. It is worth mentioning that this discussion is valid independent from the type of the crystal growth (polycrystalline or epitaxial growth). However, the density of the grain barriers can have significant effect on the conduction mechanism. In columnar and epitaxial films, the contribution of the interfaces in the overall ferroelectric properties will be dominating while If there are several grains in the structure forming in between the electrodes, then the behavior may change, leading to a less and less visible effects from the electrode interfaces part. Thus it is expected for a truly polycrystalline film to behave exactly the same as bulk ceramics, with properties dominated by the bulk and much reduced influence from the metal-ferroelectric interface.

2.6 Schottky contact

In metal like behavior materials, there is overlapping conduction and valence bands such that the Fermi level ends up within an allowed band. This means that the electron density

is very high at the Fermi level, by that making a very high electron concentration available for current flow. An electron not bound to an element is said to be at the vacuum level, having zero energy, while bound electrons have negative energies. The Fermi level E_f of a metal approximately equals to the average energy of its most energetic electrons. These electrons may be released from the metal by adding a certain energy. Electrons of a semiconductor also need some added energy to be emitted, but since the Fermi level normally is located within the forbidden gap, the required release energy is referred to the bottom of the conduction band where most of the mobile electrons are located. In this situation when these two types of materials are brought into contact with each other, there will be two possible scenarios depending on the material type. In the first place, the two materials will attain the same Fermi level in order to attain uniform chemical potential throughout the system at the state of equilibrium [40]. The level of the work function (Φ) of the metal, which is the energy difference required to excite an electron from its chemical potential (E_F) to the vacuum (E_{VAC}) with zero energy, with respect to the dopant levels in the semiconductor determines the direction of the flow of charge carriers in order to equate Fermi levels. Electrons flow from low work function material to the high work function part, in this way they also guarantee to lower their energy level. For the Schottky contact case of a metal/n-type semiconductor, where Φ_s is lower than Φ_m (See Figure 2.10-a), the surface electrons of semiconductor tend to flow to the metal surface. The flow continues until metal surface becomes negatively charged enough so as to equate the Fermi levels, resulting in a region near the semiconductor-electrode interface that is depleted of negative carriers and as a result, a positively charged impurity zone is formed. This situation causes the band-bending in semiconductor energy, lowering them with respect to the levels before the junction was made. As it can be seen in Figure 2.10, the band gap remains constant as well as the position of the band edges away from the interface. Due to the accumulation of electrons on the side of the metal-like contact, there is a positively charged region in the semiconductor as aforementioned and it is called the depletion zone. The approximately spatially uniform ionized donors are assumed to be the only source of charge in this region. Depletion zone creates a built in potential between positively charged semiconductor side and negatively charged metal side.

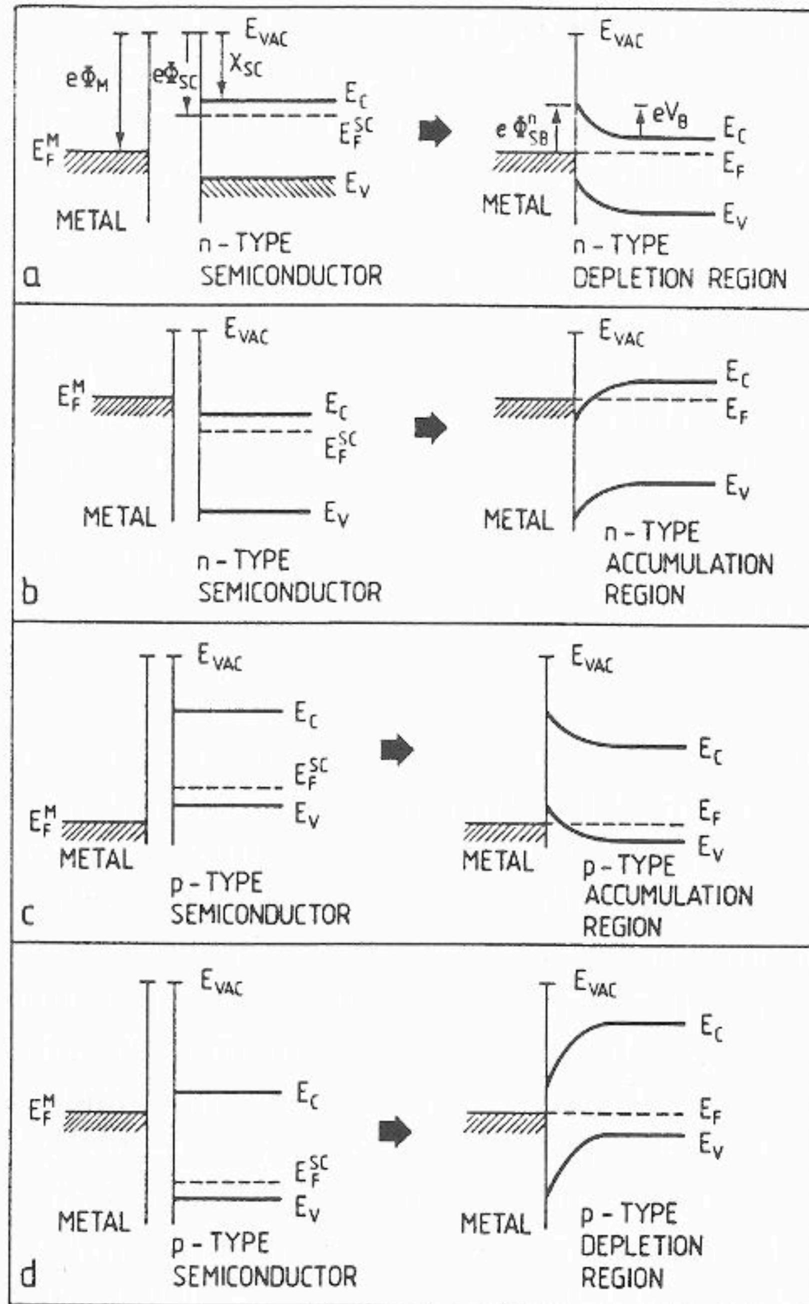

Figure 2.10: Metal-semicoductor junctions. a) High-work-function metal and *n-type* semiconductor, Schottky b) Low-work-function metal and *n-type* semiconductor, Ohmic c) High-work-function metal and *p-type* semiconductor, Ohmic d) Low-work-function metal and *n-type* semiconductor, Schottky. The energy of the bands is plotted as a function of distance z in a direction normal to the surface. E_{VAC}, vacuum energy; E_C, energy of conduction band minumum; E_V, energy of valence band maximum; E_F, Fermi level energy [41].

If the semiconductor is *p-type*, Schottky contact will be formed when Φ_s is higher than Φ_m (See Figure 2.10-d). In this case, flow of electrons will be from metal-like contact towards semiconductor. So the depletion zone will have excess of electrons and hence negatively charged. In spite of these differences, the behavior of the contact in the case of an externally applied voltage will be the same as *n-type* case: Forward bias will reduce the depletion width and reverse bias will increase. Note that terminal connections will be reversed for *p-type* and *n-type* semiconductor, i.e., when *n-type* semiconductor is connected to negative end, it creates a forward bias while *p-type* semiconductor creates a reverse bias when connected to negative end.

2.7 Ohmic contact

Figure 2.10-b exhibits another metal–*n-type* semiconductor junction, at which Φs is higher than Φ_m. In this case metal donates electron to semiconductor, enriches the region with negative charge carriers, while itself becoming slightly positive with the positive charges of the remaining of flowed electrons. As a result, the region behaves as an accumulation layer (Ohmic contact) where the carriers are free to flow in or out of the semiconductor so that there is a minimal resistance across the contact [42].

Two opposite forces establish the balance of accumulation layer in the absence of external electric field. First, a pull toward the metal since the electrons in the accumulation layer are in a region with an electric field and metal consists the positive end of this field. Second, a diffusion force towards the semiconductor since the electron density in accumulation layer is higher than the rest of the semiconductor. A steady state condition is satisfied by equilibrium of these forces.

2.8 Conduction Mechanisms in Ferroelectrics

Ferroelectrics in most of their applications are used as capacitors, either as bulk ceramics or single crystals or as thin films of polycrystalline or epitaxial quality [43,44]. Using a

ferroelectric as a capacitor creates two types of interfaces: ferroelectric/electrode and electrode/substrate. Since the conduction in a capacitor takes place through its bulk and its interfaces, the performance of the capacitor will be highly dependant on the quality of the interface [45]. Conduction mechanisms in ferroelectrics can be divided in two main parts [45,39]:

- Bulk limited: ohmic-type conduction; space charge limited currents (SCLC); Pool-Frenkel emission from the deep traps (PFE); hopping.
- Interface limited: thermionic emission over the potential barrier at the electrode interface, known also as Schottky emission (SE); electric field assisted tunnelling or Fowler-Nordheim tunneling (FNT).

In order to monitor the charge transport and understand its mechanism, we can use current-voltage (I-V) measurements. Having I-V characteristics in different temperatures, we can compare above-mentioned mechanisms with our data to see if our experimental data fits one of the known mechanisms. However, there is this possibility that more than one conduction mechanism fit the data.

For example, in one case when plotting the I-V characteristics in log-log scale we may observe that on some voltage range the slope is near unity and that on a higher voltage range the slope is near 2 (In between could be a very narrow voltage range where the slope is much higher, usually around 10). For the first guess from these data we may conclude that at low voltage the conduction is ohmic and that at high voltage the conduction is dominated by trap controlled space charge limited currents. However, the same set of experimental data may fit the Schottky emission or the Pool-Frenkel emission if we draw the $ln(I) \sim V^{1/2}$ representation.

Using measurements in different temperatures could be helpful in some of these cases since the temperature dependence is not exactly the same for all conduction mechanisms.

Another solution for this problem is to perform I-V measurements on different thicknesses of the samples since there have been reports suggesting that thickness dependency is also different in various conduction mechanisms (e.g. SCLC varies as d^{-3}, with d the thickness of the film, while the hopping is proportional with d) [46].

2.9 Ferroelectric $BiFeO_3$ Thin Film Capacitor and Its Electrical Properties

Other than antiferromagnetic properties of $BiFeO_3$ that makes it an attractive material compared to $BaTiO_3$ and PZT, the fact that the origin of the ferroelectricity in $BiFeO_3$ is electronic (lone pair) and is not strongly related to ionic displacements makes it more attractive [4]. Its band gap is around 2.8 eV, which is smaller compared to the other two. (Around 4 eV in the case of PZT and $BaTiO_3$) [16]. This is one of the reasons $BiFeO_3$ has higher leakage compared to other perovskite ferroelectric structures [47].

The influence of the polarization charge on the specific properties of the interface (built-in potential, maximum electric field, capacitance) is analyzed. Further on, the effect of the A-site doping on the electric properties of ferroelectrics, with special emphasis on potential barrier, will be discussed by comparing pure and gadolinium doped $BiFeO_3$ films.

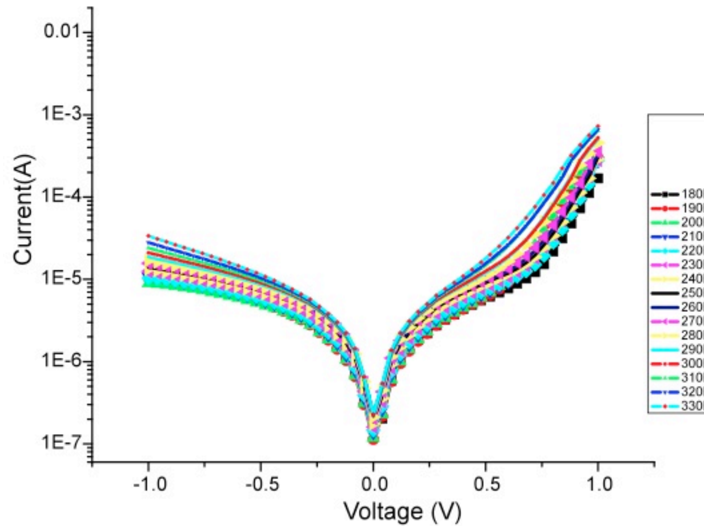

Figure 2.11: Current voltage characteristics of a single phase $BiFeO_3$ sample in different temperatures

As it can be seen in Figure 2.11, the temperature dependence is weak for both polarities. The diode-like behavior suggests that the conduction mechanism is controlled by electrode interfaces, at least on one side. Analysis is done for the negative part assuming Schottky emission [39]:

$$J = A^{*}T^{2}\exp(-\frac{q}{kT}(\Phi_{B}^{0} - \sqrt{\frac{qE_{m}}{4\pi\varepsilon_{0}\varepsilon_{op}}}))$$

Equation 2.4: The Schottky emission equation where q is the electron charge, k is the Boltzmann's constant, T is the temperature, $\Phi_B{}^0$ is the potential barrier at zero bias, E_m is the maximum field at the interface if a Schottky-like contact is present, ε_0 is the vacuum permittivity and ε_{op} is the dielectric constant at optical frequencies.

Schottky representation at constant voltage is:

$$Ln(\frac{J}{T^{2}}) = Ln(A^{*}) - \frac{q}{kT}\Phi_{app} \quad (2.5)$$

Using the Equation 2.5, Figure 2.12 is the represented graph of the Schottky emission.

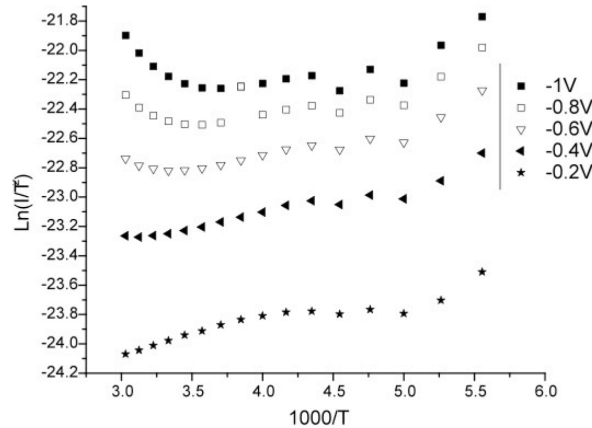

Figure 2.12: Schottky representation at constant voltage

It is clear that Schottky emission is not the right conduction mechanism. To confirm these, we have also tested the Schottky representation at constant temperature:

$$L(\frac{J}{T^2}) \sim (Ln(A^*) - \frac{q\Phi_B^0}{kT}) - f(V^{1/2})$$

Equation 2.6: The equation for Schottky representation at constant temperature

The term in the brackets was noted as *F(T)*:

$$F(T) \sim Ln(A^*) - \frac{q\Phi_B^0}{kT} \quad (2.7)$$

Examples of Schottky representations at constant temperature are shown below.

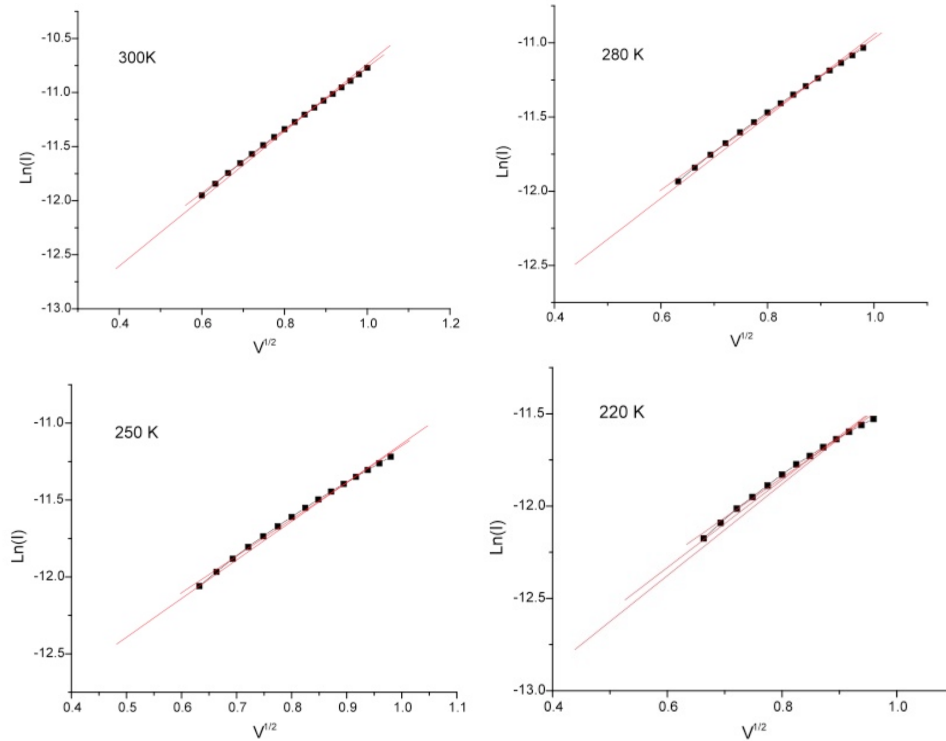

Figure 2.13: Examples of Schottky emission at constant temperature

In our case, although the linear fit is good, at least for voltages above 0.4 V, taking the intercept *F(T)* and representing as function of *100/T* it can be seen that this is almost temperature independent (See Figure 2.14). This fact confirms that the Schottky emission is not the right conduction mechanism for negative polarity in single phase $BiFeO_3$.

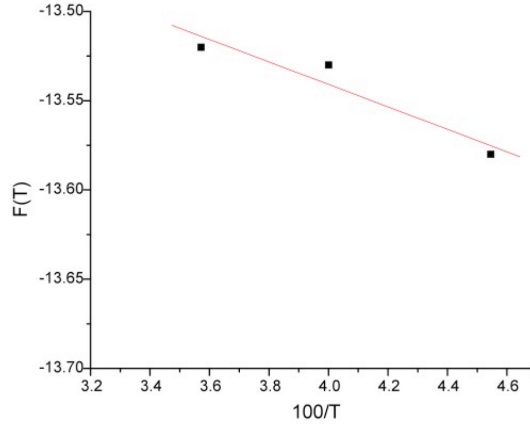

Figure 2.14: Temperature independency in *F(T)* versus *100/T*

A $V^{1/2}$ dependence has the current density in the case of Pool-Frenkel emission. The slope of the $Ln(I) \sim V^{1/2}$ representation at constant temperature, in the case of Pool-Frenkel emission, should give the optical dielectric constant if the thickness of the film is known. Carrying out calculations with the approximation (via SEM images) that the film thickness is 100nm, the slope gives a value around 4 for ε_{op}, which is quite plausible. The activation energy can be estimated from the slope of the Arrhenius representations at constant voltage, shown Figure 2.15.

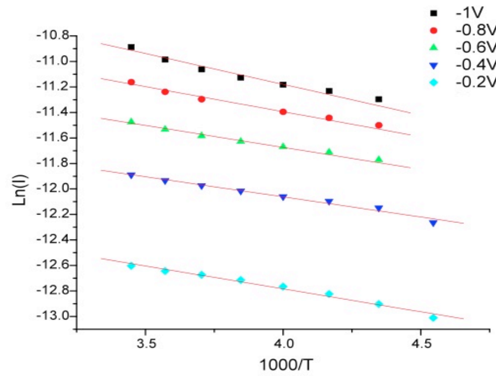

Figure 2.15: Arrhenius representations at constant voltage

The activation energy for the emitting trap should be dependent on voltage as $V^{1/2}$ (the Pool-Frenkel effect). We did this representation shown in Figure 2.16.

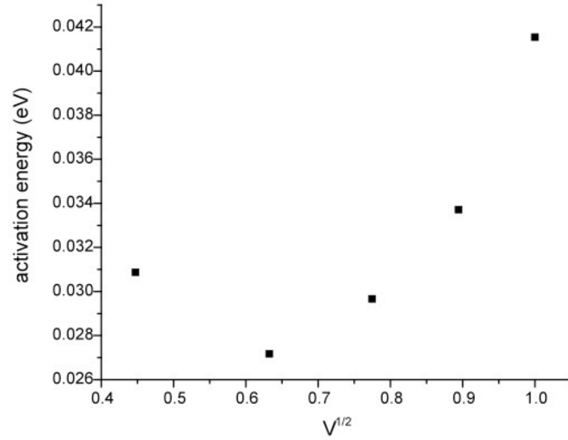

Figure 2.16: Activation energy versus $V^{1/2}$

It can be seen that the “activation energy” has no dependency on $V^{1/2}$ and it is very small.

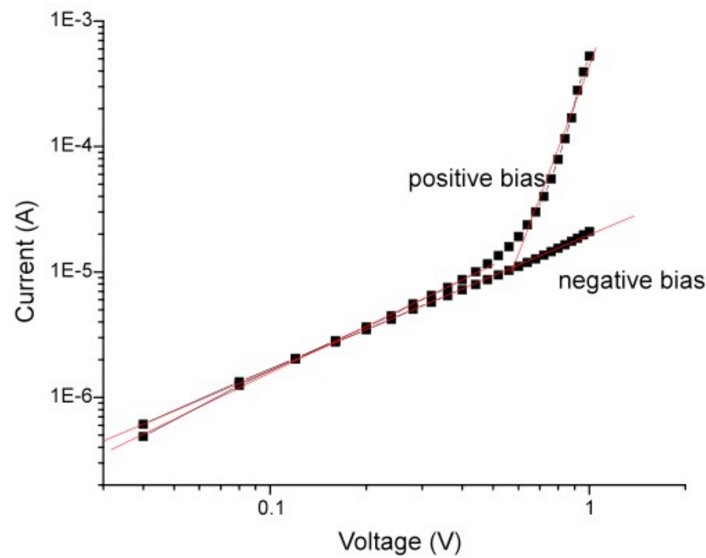

Figure 2.17: The log-log representation for the I-V characteristics of $BiFeO_3$ sample at 300K

The Figure 2.17 is the simple log-log representation for the I-V characteristic at 300K. Surprisingly, for negative bias the slope is 1.01 suggesting a clear ohmic behavior. For positive bias, the slope is about 1.2 at low voltages and increases at about 6 at high voltage. This fact indeed suggests a combination of ohmic and SCLC mechanisms in single phase $BiFeO_3$.

Results for 5% Gd doped samples:

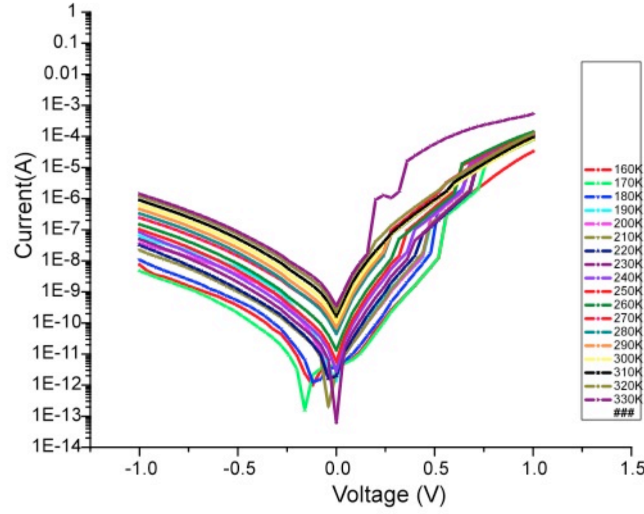

Figure 2.18: Current voltage characteristics of a 5% Gd doped $BiFeO_3$ sample in different temperatures

In this case there is a clear temperature dependence on the negative side, of more than 3 orders of magnitude. The diode-like behavior is still present, although it is possible that on the positive side the current behavior is combination of ohmic and SCLC as for single phase $BiFeO_3$. It can be assumed that the $SrTiO_3$:Nb/$BiFeO_3$(5%Gd)/Pt structure behaves almost as a single Schottky-like diode. This is reverse biased when negative polarity is on the top Pt contact and is forward biased for positive polarity on top. However, it is not known that, which electrode interface is the good Schottky contact and which one is the bad Schottky or ohmic contact.

Schottky-Simmons equation for the negative side:

$$J = 2q\left(\frac{2\pi m_{eff} kT}{h^2}\right)^{3/2} \mu E \exp\left(-\frac{q}{kT}\left(\Phi_B^0 - \sqrt{\frac{qE_m}{4\pi\varepsilon_0\varepsilon_{op}}}\right)\right) \qquad (2.8)$$

The useful representation is given in Equation 2.9:

$$\ln\left(\frac{J}{T^{3/2}}\right) = \ln\left(2q\left(\frac{2\pi m_{eff} kT}{h^2}\right)^{3/2} \mu E\right) - \frac{q}{kT}\left(\Phi_B^0 - \sqrt{\frac{qE_m}{4\pi\varepsilon_0\varepsilon_{op}}}\right) \quad (2.9)$$

Thus, representing *ln(I/T^3/2^)~1000/T,* we should obtain some lines, and from the slopes we get the apparent potential barriers. The representation is shown in Figure 2.19.

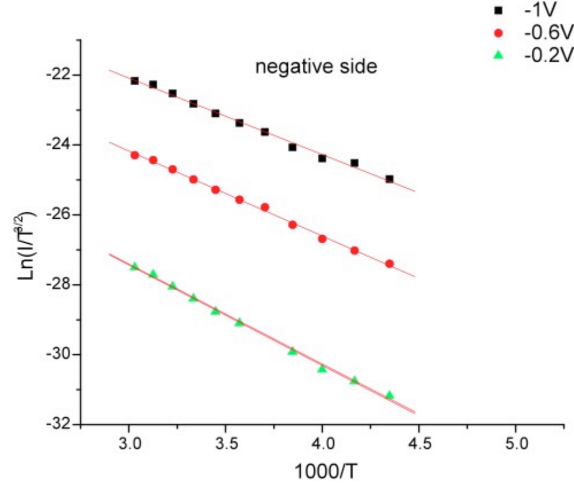

Figure 2.19: $\ln(I/T^{3/2})\sim 1000/T$ representation

Further on, the apparent potential barrier should be voltage dependent. The dependence is either $V^{1/2}$, if $\sqrt{2qN_{eff}V/\varepsilon_0\varepsilon_{st}} << P/\varepsilon_0\varepsilon_{st}$, or is $V^{1/4}$ if $\sqrt{2qN_{eff}V/\varepsilon_0\varepsilon_{st}} >> P/\varepsilon_0\varepsilon_{st}$ [39]. In the present case we suspect actual magnitude of the polarization because it is small because is screened by the high leakage. Therefore we will consider the $V^{1/4}$ dependence. We represented the apparent potential barrier as function of $V^{1/4}$ and from the intercept at the origin we obtained the potential barrier at zero bias, which is of about 0.45 eV (See Figure 2.20).

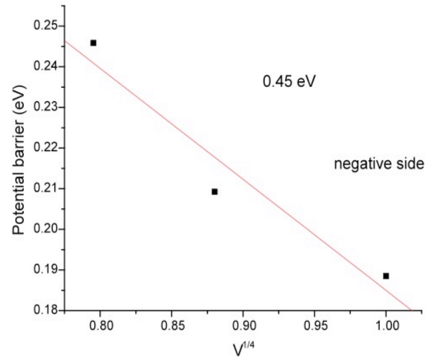

Figure 2.20: apparent potential barrier as function of $V^{1/4}$

The same procedure done on 10% Gd doped $BiFeO_3$. Followings are the results:

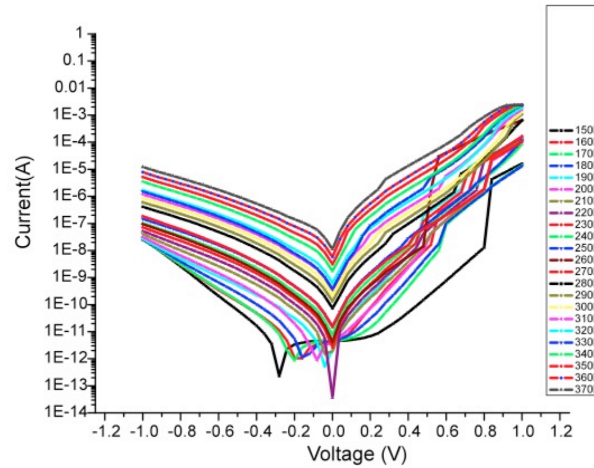

Figure 2.21: Current voltage characteristics of a 10% Gd doped $BiFeO_3$ sample in different temperatures

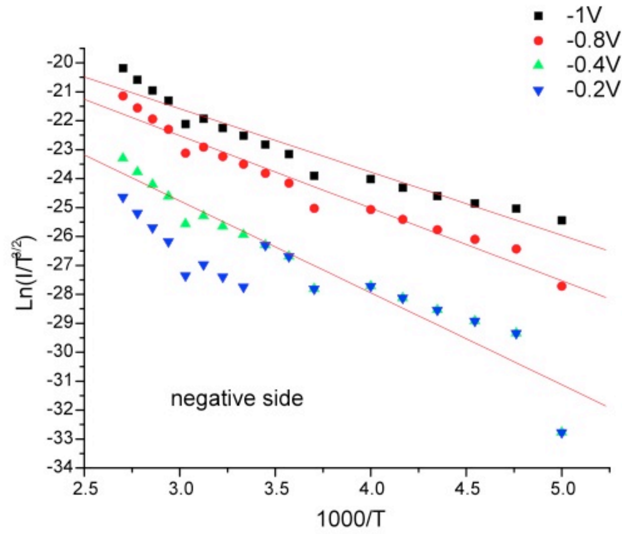

Figure 2.22: $ln(I/T^{3/2})\sim 1000/T$ representation

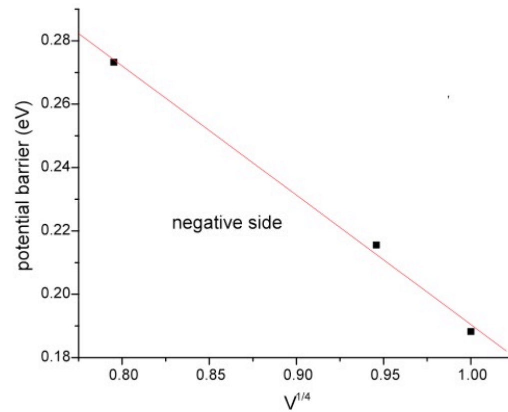

Figure 2.23: Apparent potential barrier as function of $V^{1/4}$

For 10% gd doped $BiFeO_3$ the barrier is almost 0.6 eV.

Referring strictly to the $SrTiO_3$:Nb/$BiFeO_3$/Pt structures it can be claimed that: For single phase $BiFeO_3$, the leakage is high and the conduction is mainly ohmic.

For Gd doped $BiFeO_3$ one of the interface act as a Schottky contact, while the other remains a weak rectifying contact, almost ohmic. The potential barrier seems to increase

with the Gd doping, as its values changes from about 0.45 eV at 5 % Gd to about 0.6 eV at 10 % Gd.

The diode like behavior is supported also by the C-V. We represented $1/C^2 \sim V$ as for a Schottky diode in the case of $BiFeO_3$ with 5 % Gd (See Figure 2.24).

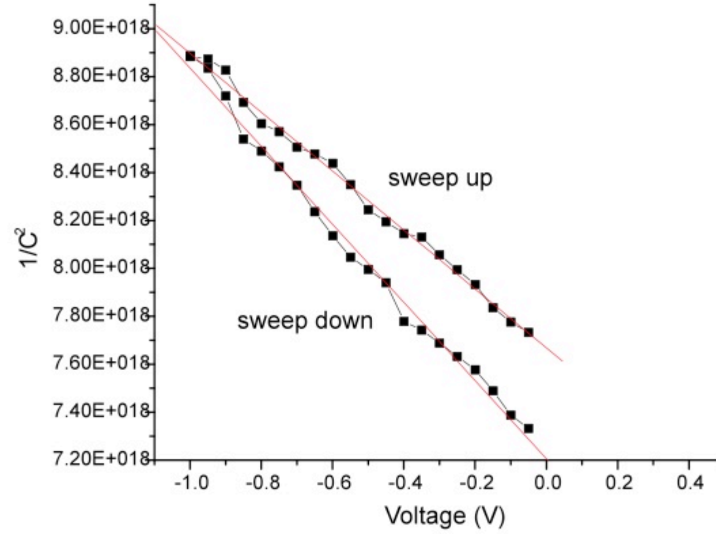

Figure 2.24: $1/C^2$ versus V diagram in 5% Gd doped $BiFeO_3$

The dependence is linear, as it should be. The fact that the two lines are not overlapping is a sign that $BiFeO_3$ has some ferroelectricity. The built-in potential is different for the two orientations of polarization. Also, the slope is different, suggesting a different concentration of charges in the depleted region for the two orientations of polarizations.

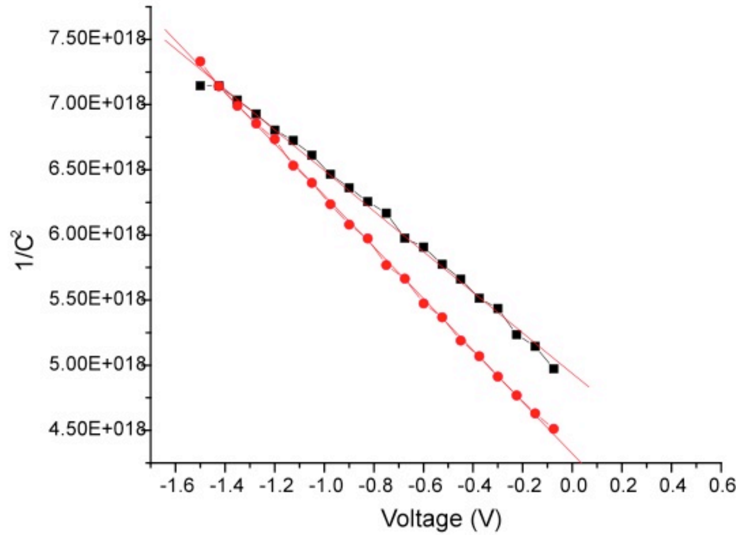

Figure 2.25: $1/C^2$ versus V diagram in 10% Gd doped $BiFeO_3$

Figure 2.25 confirms the same for 10% Gd doped $BiFeO_3$. Therefore, with Gd we have a nice Schottky diode or more exactly an n^+-p Schottky like diode, most probably between $SrTiO_3$:Nb and Gd doped $BiFeO_3$, assuming that Gd makes the $BiFeO_3$ p-type [48]. Several methods were tested to reduce the leakage with varying degrees of success. Among them was doping with iso- or heterovalent atoms replacing Bi or Fe in $BiFeO_3$ lattice, such as La, Nb, Ca, Mn, Cr, Gd [49,50,51,12,22]. Gadolinium is particularly of interest due to the fact that it may induce some ferromagnetic activity in bismuth ferrite and that is more attractive for applications compared to the antiferromagnetic order, which is specific for pure $BiFeO_3$.

Interesting electric properties were reported for Gd doped $BiFeO_3$ films deposited by metal organic decomposition on platinized Si wafers [52]. On the other hand it was reported that the leakage current in epitaxial $BiFeO_3$ layers deposited by pulsed laser deposition (PLD) on single crystal $SrTiO_3$ substrates with $SrRuO_3$ buffer layer can be manipulated by engineering the potential barrier at the electrodes with the orientation of the $BiFeO_3$ layer. It was found that the potential barrier for $BiFeO_3$ on (100) substrates was lower than in the case of $BiFeO_3$ on (111) substrates [53]. Also, it was reported that $BiFeO_3$ deposited directly on Nb doped conducting $SrTiO_3$ single crystal substrates (Nb:$SrTiO_3$, or shortly STON) with Pt top electrode leads to a structure with diode-like

behavior. Despite the very recent interest in such structures, to our knowledge, there are no studies reporting neither on the height of the potential barrier at the STON-BFO interface nor the dopant dependence of the potential barrier and whether this barrier could be engineered by doping the $BiFeO_3$ layer.

In the present study we report on the modification of the barrier height by Gd doping of the $BiFeO_3$ layer in a Nb:$SrTiO_3$-$Bi_{(1-x)}Gd_xFeO_3$-Pt (STON-BFGO-Pt) structure with [001] direction of STON perpendicular to the plane (x=0, 0.05, 0.1). The BFGO layer was prepared by sol-gel deposition on single crystal STON substrates with (001) orientation and 0.7 % Nb doping. The structural characterization of the $BiFeO_3$ film was performed by X-ray diffraction (XRD, BrukerAxs) and it was found that the layer grows quasi-epitaxially on the single crystal substrate. The top Pt contacts of 0.1x0.1 mm^2 were deposited by magnetron RF-sputtering through a shadow mask. The electric measurements were performed at different temperatures by inserting the samples in a cryogenic probe station from LakeShore (model CPX-VF). The capacitance of the samples were measured with a Hioki LRC bridge, the leakage current with a Keithely 6517 electrometer and the hysteresis loop with a TF2000 ferroelectric tester from AixAcct.

Polarization-applied field measurements showed that the hysteresis loops both in pure and doped $BiFeO_3$ were severely distorted by the leakage current even at temperatures lower than room temperature (RT). The ferroelectric behavior of the $BiFeO_3$ layers could be confirmed only by capacitance-voltage (C-V) characteristics as shown in the Figure 2.26.

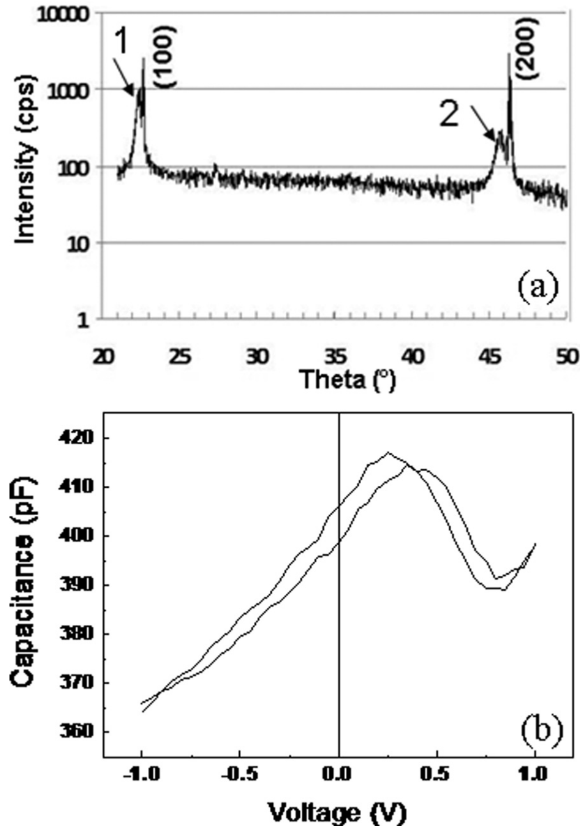

Figure 2.26: (a) XRD pattern of the pure $BiFeO_3$ film where 1 and 2 denote (100) and (200) peaks of the film, respectively. Note that Gd doped films have nearly the same pattern (not shown here), (b) C-V characteristics at room temperature for single phase $BiFeO_3$ layer. Measurement performed at 100kHz with amplitude of 0.1V for ac signal.

The C-V curves in Figure 2.26 presents the butterfly shape specific for ferroelectrics. The shift between the sweep-up and sweep-down characteristics is small, suggesting a small coercive field and a relatively small value for the remnant polarization. This is possible due to the large leakage current screening the ferroelectric polarization.

Following the C-V measurements, we also focused on the current-voltage (I-V) characteristics with the aim to obtain information about the dominant conduction mechanism and to evaluate the potential barrier(s) in the STON-BFGO-Pt structure. As explained in the film fabrication section, bismuth ferrite was fabricated on 0.7% niobium doped $SrTiO_3$ substrates with (100) orientation. 0.7% niobium doping makes the substrate conductive (not a metal but a degenerated semiconductor with metallic like behavior) so that the substrate can act as bottom electrode in electrical measurements. A

layer of Pt was pasted on the top of films using shadow mask to form the top electrode in electrical characteristics.

The electrical measurements were done on $SrTiO_3$:Nb/$BiFeO_3$/Pt structures where bismuth ferrite was doped with different levels of gadolinium doping. Three samples were used for I-V measurements:

- Single phase $BiFeO_3$
- $BiFeO_3$ doped with 5 % Gd
- $BiFeO_3$ doped with 10 % Gd

The room temperature I-V characteristics are presented in the Figure 2.27 for pure and doped $BiFeO_3$ (5 and 10%).

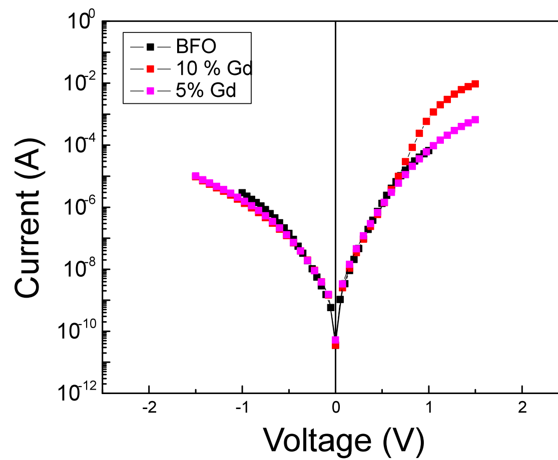

Figure 2.27: I-V characteristics at room temperature for different Gd doping of the $BiFeO_3$ layer.

The 5% Gd doping makes no difference where in higher doping level (10% Gd doping) it seems to have some impact only on the positive polarity.

The I-V results are for measurements done at room temperature. Since the electrodes on the top and bottom of the film layers are different, there is an asymmetry in the curves. The curves exhibit the diode like behavior in all cases. Apart from that, the heavy asymmetry in the I-V curve in Figure 2.27 shows that the $SrTiO_3$:Nb/$BiFeO_3$/Pt structure

has a diode like behavior, being forward biased for positive voltages applied on the top Pt contact and reverse biased for negative voltages applied on Pt. Apparently the current magnitude does not vary much with the Gd doping. The rectification ratio is not very large for this case, being around 40 at +/- 1 V.

In order to gain further insights, the I-V characteristics at different temperatures were performed on pure and doped $BiFeO_3$ layers. The results are given in Figure 2.28.

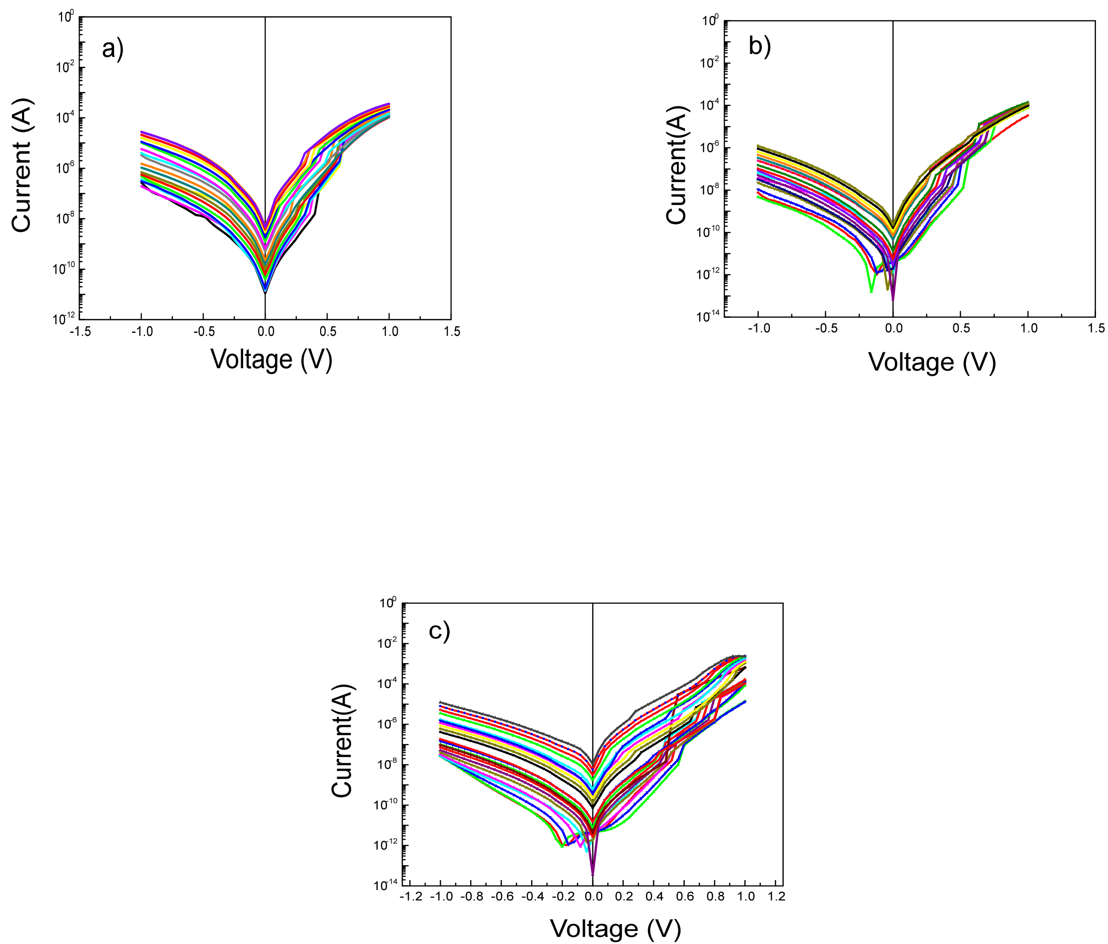

Figure 2.28: I-V characteristics at different temperatures for $BiFeO_3$ films with no Gd doping (a), with 5 % Gd doping (b) and with 10 % Gd doping (c).

From Figure 2.28, it is clear that, for the negative polarity there is a great temperature dependence of the leakage current, of about 2 orders of magnitude or more at a voltage of -1 V. On the other hand, on the positive polarity side, the temperature dependence is more evident at low voltages, below 0.6 V. At higher voltages the temperature dependence diminishes, and the steps occurring in the I-V characteristics at certain voltages support the hypothesis that the leakage current for forward bias at high voltages is dominated by space charge limited currents (SCLC) possibly with exponential increase of trap emission.

In the following paragraphs, only the negative part of the I-V characteristics will be analyzed in detail in order to extract information regarding the dominant conduction mechanism for reverse bias. The rectifying behavior of the $SrTiO_3$:Nb/$BiFeO_3$/Pt structure suggests that thermionic emission over a potential barrier may be responsible for the leakage current in reverse bias.

The question is the following: "Is the potential barrier located at the $SrTiO_3$:Nb/$BiFeO_3$ interface or at the $BiFeO_3$/Pt interface?"

It could be that potential barriers exist at both interfaces but one of them is more permeable to charge injection than the other, thus leading to the diode-like I-V behavior. Another unknown is the conduction type of $BiFeO_3$ in bulk of the film. Previous reports suggest p-type conduction due to bismuth losses during PLD deposition or during crystallization annealing in the case of sol-gel deposited films (See Figure 2.29) [48]. Recent X-ray photoelectron spectroscopy studies also support the idea that $BiFeO_3$ has p-type conduction [28]. Therefore, assuming that the $BiFeO_3$ films in the present study are also p-type, the reverse bias occurs when the negative voltage is applied on the top Pt electrode, meaning positive polarity on the bottom single crystal $SrTiO_3$:Nb substrate. Therefore, it can be concluded that the reverse biased Schottky contact is located at the bottom $SrTiO_3$:Nb/$BiFeO_3$ interface while the top $BiFeO_3$/Pt interface behaves as a quasi-ohmic contact.

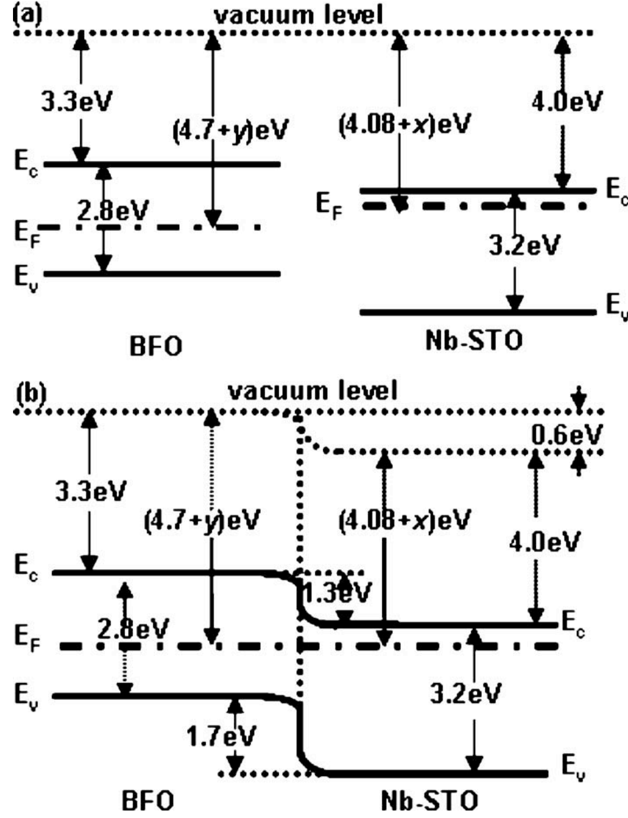

Figure 2.29: (a) Energy band diagram of isolated $BiFeO_3$ and Nb-STO semiconductors. (b) Energy band diagram of an ideal BFO/Nb-STO p-n heterojunction at thermal equilibrium [48].

With the above proposition in mind, the temperature dependence of the negative part of the I-V characteristics presented in Figure 2.28 was analyzed considering a conduction mechanism in which the injection of charge is controlled by the potential barrier existing at the $SrTiO_3$:Nb/$BiFeO_3$ interface while the drift throughout the ferroelectric film is controlled by the bulk. The Schottky-Simmons equation was used [54]:

$$J = 2q\left(\frac{2\pi m_{eff} kT}{h^2}\right)^{3/2} \mu E \exp\left(-\frac{q}{kT}\left(\Phi_B^0 - \sqrt{\frac{qE_m}{4\pi\varepsilon_0\varepsilon_{op}}}\right)\right) \qquad (2.10)$$

Equation 2.11 is the Schottky-Simmons equation where q is the electron charge, h is the Planck's constant, m_{eff} is the effective mass, k is the Boltzmann's constant, μ is the mobility of electrons in the conduction band of $BiFeO_3$, E is the electric field in the bulk of $BiFeO_3$, T is the temperature, $\Phi_B{}^0$ is the potential barrier at zero bias, E_m is the

maximum field at the interface if a Schottky-like contact is present (with a depletion region having a voltage dependent width), ε_0 is the vacuum permittivity and ε_{op} is the dielectric constant at optical frequencies.

E_m is given by [39]:

$$E_m = \sqrt{\frac{2qN_{eff}(V + V'_{bi})}{\varepsilon_0 \varepsilon_{st}}} + \frac{P}{\varepsilon_0 \varepsilon_{st}} \tag{2.12}$$

Equation 2.13 shows the maximum field at the interface (E_m) where Neff is the effective density of charge in the depleted region of the Schottky type contact, P is the ferroelectric polarization, Vbi is the built-in potential (including the contribution of ferroelectric polarization), and εst is the static dielectric constant.

Depending on the term dominating the value of E_m the current density J from

(2.10)

will be a function of either the square root or ¼th power of applied voltage. If the polarization term is dominant $(\sqrt{2qN_{eff}(V + V'_{bi})/(\varepsilon_0 \varepsilon_{st})} << P/(\varepsilon_0 \varepsilon_{st}))$ then $log J \propto V^{1/2}$ and the potential barrier at zero volt Φ_B^0 is drastically reduced by the ferroelectric polarization. If the polarization term is negligible in the Equation 2.12, then $log J \propto V^{1/4}$ is valid. It must be noted that Equation 2.12 applies if the ferroelectric film is only partially depleted in the voltage range employed for electrical measurements. Referring to the samples studied in this work, it is clear that pure and doped $BiFeO_3$ layers are partially depleted in the voltage range used for C-V measurements (See Figure 2.26) as the capacitance varies continuously with the applied voltage. In the case of a fully depleted film the capacitance should converge towards a constant value with increasing the voltage, which is definitely not the case. Moreover, considering the difficulty to record a polarization hysteresis and small voltage difference between the maxima of the sweep-up and sweep-down curves in C-V measurements and the high magnitude of the leakage current it can be assumed that remnant polarization is small in the $BiFeO_3$ layer and that the polarization term in Equation 2.12 is negligible. Another contribution comes from the possibly large value of ε_{st} in our films which is often reported to be large in sol-gel films

due to texturing and N_{eff} is also usually larger than in epitaxial films. Therefore, it is reasonable to consider the case $lnJ \sim V^{1/4}$. The data were analyzed in the following way:

The term $ln(J/T^{3/2})$ was plotted as a function of $1000/T$ (Arrhenius plot) for a certain applied voltage, and from the slope the potential barrier at the relevant bias voltage was estimated (including the Schottky effect). The potential barriers at several applied voltages were then plotted as a function of $V^{1/4}$ and the potential barrier at zero volts was estimated from the intercept at the origin. Here, the better is the linear fit, the more accurate is the estimate of Φ_B^0. However, an error up to 0.1 eV is possible while applying this method. The $V^{1/4}$ dependence of the potential barrier is presented in the figure 4 for the $BiFeO_3$ samples with different Gd content.

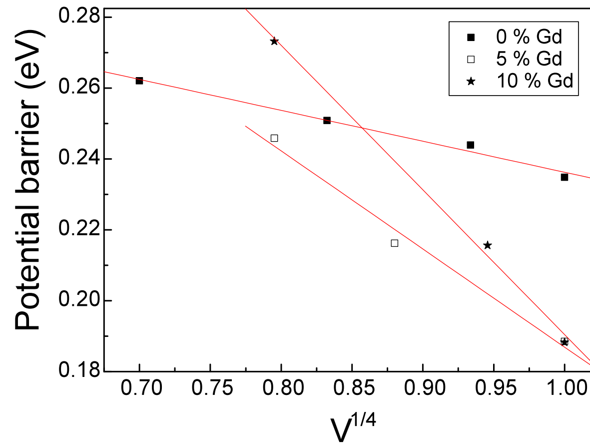

Figure 2.30: The voltage dependence of the potential barrier in the case of $BiFeO_3$ films with different Gd doping, on $SrTiO_3$:Nb substrates. The confidence factor for the linear fit is in all cases higher than 0.99.

The intercept at the origin yields the following values for the potential barrier at zero volts:

0.32 eV at zero doping

0.45 eV for 5 % Gd doping

0.60 eV for 10 % Gd doping

The results show that the height of the potential barrier increases with increasing the Gd content in the $BiFeO_3$ films. This is a very interesting result, which can be explained assuming a compensation mechanism of the holes introduced by the presence of Bi vacancies, by the electrons introduced via Gd doping. In the un-doped $BiFeO_3$ films the conduction is predominantly p-type, the Fermi level is closer to the valance band, thus the potential barrier for holes is not very high. The Gd doping can compensate the p-type conduction, thus the Fermi level moves towards the middle of the forbidden band leading to an increase in the potential barrier for holes.

However, in spite of significant increasing in the potential barrier, the magnitude of the leakage current on the negative side of the I-V characteristics does not vary significantly with the Gd doping. Referring to the Equation 2.10, it can be seen that a quantity, which may impact significantly the apparent potential barrier and the carrier injection into the ferroelectric layer is the maximum field at the interface E_m. There are several quantities, which can vary with the Gd content, such as N_{eff}, P, V_{bi} and ε_{st}. Therefore, it is hard to decide which of these quantities is contributing the most to the partial compensation of the increased barrier height.

Some useful information can be extracted from the C-V characteristics, assuming that the $BiFeO_3$ film behaves as a wide gap semiconductor. The $1/C^2$-V representation can be used to extract information about the density of the free carriers. Figure 2.31 shows the above representation for the case of pure $BiFeO_3$ film. Similar results were obtained for the films doped with 5 % and 10 % Gd.

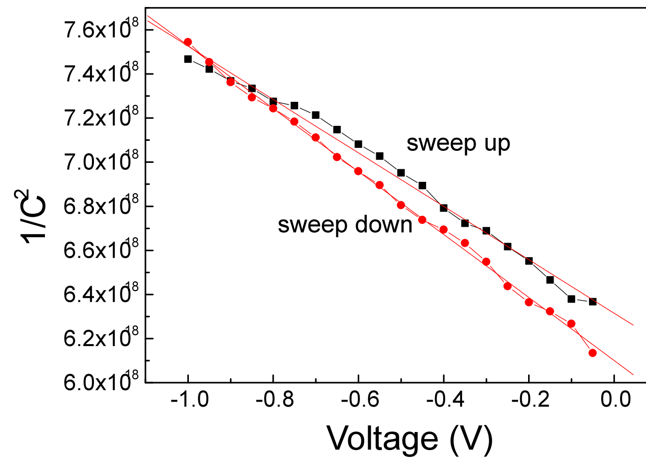

Figure 2.31: The $1/C^2$ representation for the pure $BiFeO_3$ film.

In Figure 2.31, one has to notice that the intercept at origin on the voltage axis, giving the built in potential V_{bi}, is not the same for sweep-up and sweep-down. This fact is a fingerprint for the presence of the ferroelectric polarization, which is changing the band bending at the interface depending on the sign of the polarization charge. The slope of the $1/C^2 \sim V$ dependence was used to estimate the density of the free carriers n, and the intercept was used to extract the built-in potential V_{bi}. The results are presented in the Table 2.1.

Table 2.1- The estimated values for the density of free carriers n and for the built-in potential V_{bi} for different values of the Gd doping. The estimates were performed considering a thickness of about 200nm for the $BiFeO_3$ films and a value of 800 for the static dielectric constant. The last value is based on the fact that the capacitance value at -1V is about the same for all samples.

Gd doping	0 %		5 %		10 %	
	n (cm^{-3})	V_{bi} (V)	n (cm^{-3})	V_{bi} (V)	n (cm^{-3})	V_{bi} (V)
Sweep up	1.44×10^{19}	0.26	1.43×10^{19}	0.4	1.13×10^{19}	0.46
Sweep down	1.23×10^{19}	0.06	1.08×10^{19}	0.015	8.9×10^{18}	0.026

It can be seen that the density of the free carriers is slightly decreasing with increasing the level of Gd doping, supporting the hypothesis of the compensation of the p-type conduction by introducing electrons from the doping.

However, it has to be underlined that N_{eff} is not the same with n, as N_{eff} accounts for the density of the fixed charge, namely ionized impurities, in the depletion region of the Schottky contact while n is the density of the free carriers. N_{eff} can be larger than n because of the trapped charges in the depleted region.

The difference in n for sweep-up and sweep-down can give an estimate for 2P, considering that this is the charge compensating the polarization. The obtained value for 2P is between 6 and 11 $\mu C/cm^2$, confirming that the polarization is very low because of the screening produced by the high density of free carriers.

Chapter 3 CONCLUDING REMARKS AND FUTURE WORK

3.1 Conclusion

A sol-gel method was used to synthesize strongly textured or near-epitaxial $BiFeO_3$ films in single-phase on (001) Nb doped $SrTiO_3$ substrates. First, effects of Gd doping on structure and transition temperature in bulk form followed by leakage current in film form were investigated. Powder X-ray diffraction results indicated that cubic perovskite phase formed without secondary phases up until 10% Gd. Doping with Gd lowered the ferroelectric-paraelectric transition temperature with respect to bulk. Thin films had a strong texture where only peaks near the substrate ones were present. Same precursor for bulk synthesis was used to thin film fabrication. Electrical characterization work suggests that modifying BiFeO3 with Gd can significantly reduce leakage current, a prominent problem in BiFeO3 films. It was shown that the potential barrier at the SrTiO3:Nb-BiFeO3 interface can be engineered by Gd doping. The height of the potential barrier and the built-in bias increases with Gd doping. While the concentration of the free carriers in the BiFeO3 layer decreases, the leakage current remains still too large to record a hysteresis loop. This is because the reduction of the barrier height and the increase of the built-in potential have opposite effects on the current density according to the Equation 2.10 and Equation 2.12. Further studies are needed to fully elucidate the origin of the high conductivity in pure BiFeO3 films. Only in this way the compensation mechanism by doping can be effective in the reduction of the leakage current.

3.2 Future Work

Other elements with properties close to Gd could be used as doping element to investigate if they will give rise to some magnetic activity of the otherwise antiferromagnetically ordered $BiFeO_3$ phase. Among them are La, Ca and Sm which will act as A-site and B-site elements in the perovskite structure. Controlling the leakage currents might also make it possible along with magnetic ordering design of materials for spintronics or spin valves. They might also stabilize Bi as Bi is proven to be a volatile element leaving A-site positions and creating charge carriers, which destroys any benefit from ferroelectricity in perovskite $BiFeO_3$. The same study could be done using other film fabrication methods such as Pulsed Laser Deposition (PLD) to see haw different fabrication methods affects the electrical properties as well as structural quality. Effect of doping elements with $BiFeO_3$ on the microstructure can be investigated considering that there were observations in this study suggesting different physical properties in various levels of doping and doped elements.

Bibliography

1. UCHINO, K. **Ferroelectric devices**. [S.l.]: CRC, v. 16, 2000.

2. LINES, M. E.; GLASS, A. M. **Principles and applications of ferroelectrics and related materials**. [S.l.]: Oxford University Press, USA, 2001.

3. COLOGLU, H. N. **PHASE TRANSITIONS INTO MULTIDOMAIN STATES IN FERROELECTRIC THIN FILMS WITH DEPLETION CHARGES AND PARTIAL ELECTRODE SCREENING**. Sabanci University. [S.l.]. 2011.

4. PINTILIE, L. Charge Transport in Ferroelectric Thin Films. [S.l.]: [s.n.].

5. DAMJANOVIC, D. Ferroelectric, dielectric and piezoelectric properties of ferroelectric thin films and ceramics. **Reports on Progress in Physics**, v. 61, p. 1267, 1998.

6. TAGANTSEV, A. K.; GERRA, G. Interface-induced phenomena in polarization response of ferroelectric thin films. **Journal of applied physics**, v. 100, p. 051607, 2006.

7. TAGANTSEV, A. K. et al. Non-Kolmogorov-Avrami switching kinetics in ferroelectric thin films. **Physical Review B**, v. 66, 2002.

8. SHUR, V. Y. et al. Polarization reversal in congruent and stoichiometric lithium tantalate. **Applied Physics Letters**, v. 79, 2001.

9. LOHSE, O. et al. Relaxation mechanism of ferroelectric switching in Pb (Zr, Ti) O thin films. **Journal of Applied Physics**, v. 89, 2001.

10. JIANG, A. Q.; LIN, Y. Y.; TANG, T. A. Interfacial-layer modulation of domain switching current in ferroelectric thin films. **Journal of applied physics**, v. 101, 2007.

11. YUAN, G. L. et al. Preparation and multi-properties of insulated single-phase BiFeO3 ceramics. **Solid State Communications**, v. 138, p. 76-81, 2006.

12. JIANG, Q. H.; NAN, C. W.; SHEN, Z. J. Synthesis and properties of multiferroic la-modified BiFeO3 ceramics. **Journal of the American Ceramic Society**, 2006.

13. KARTAVTSEVA, M. S. et al. BiFeO3 thin films prepared using metalorganic chemical vapor deposition. **Thin solid films**, v. 515, p. 6416, 2007.

14. SHVARTSMAN, V. V. et al. Large bulk polarization and regular domain structure in ceramic BiFeO3. **Applied Physics Letters**, v. 90, p. 172115, 2007.

15. MARTIN, L. W. **Engineering multiferroic materials and new functionalities in materials**. [S.l.]: ProQuest, 2008.

16. WANG, J. et al. Epitaxial BiFeO3 Multiferroic Thin Film Heterostructures. **Science**, v. 299, p. 1719-1722, 2003.

17. YUN, K. Y.; NODA, M.; OKUYAMA, M. Prominent ferroelectricity of BiFeO3 thin films prepared by pulsed-laser deposition. **Applied physics letters** , v. 83, p. 3981, 2001.

18. DAI, Z.; AKISHIGE, Y. Electrical properties of multiferroic BiFeO3 ceramics synthesized by spark plasma sintering. **J. Phys. D: Appl. Phys**, 2010.

19. WU, Z.; COHEN, R. E. Pressure-Induced Anomalous Phase Transitions and Colossal Enhancement of Piezoelectricity in PbTiO3. **Physical review letters**, v. 95, p. 37601, 2005.

20. CATALAN, G.; SCOTT, J. F. Physics and applications of bismuth ferrite. **Advanced Materials**, v. 21, p. 2463--2485, 2009.

21. KALININ, S. V. et al. Potential and impedance imaging of polycrystalline BiFeO3 ceramics. **Journal of the American Ceramic Society**, v. 85, p. 3011--3017, 2002.

22. PALKER, V. R. et al. Magnetoelectricity at Room Temperature in the Bi(0.9-x)Tb(x)La(0.1)FeO3 System. **Phys. Rev.**, 2004.

23. KIM, J. K.; KIM, S. S.; KIM, W. J. Sol-gel synthesis and properties of multiferroic BiFeO3. **Materials Letters**, 2005.

24. KUMAR, M. M. et al. Ferroelectricity in a pure BiFeO ceramic. **Applied Physics Letters**, v. 76, p. 2764, 2000.

25. XU, J. H. et al. Low-temperature synthesis of BiFeO3 nanopowders via a sol-gel method. **Journal of Alloys and Compounds**, v. 472, p. 473--477, 2009.

26. GONZALEZ GARCIA, F.; RICCARDI, C.; SIMOES, A. Lanthanum doped BiFeO3 powders: Syntheses and characterization. **Journal of Alloys and Compounds**, 2010.

27. CHENTIR, M. T. et al. Leakage current evolution versus dielectric thickness in lead

zirconate titanate thin film capacitors. **Journal of Applied Physics**, v. 105, 2009.

28. PINTILIE, L. et al. Orientation-dependent potential barriers in case of epitaxial Pt-BiFeO3-SrRuO3 capacitors. **Applied Physics Letters**, v. 94, n. 23, 2009.

29. MEYER, R. et al. Dynamic leakage current compensation in ferroelectric thin-film capacitor structures. **Applied Physics Letters**, v. 86, 2005.

30. TANG, X. G. et al. Leakage current and relaxation characteristics of highly (111)-oriented lead calcium titanate thin films. **Journal of applied physics**, v. 94, 2003.

31. NUNEZ, M.; BUONGIORNO NARDELLI, M. Interface phase and tuning of polarization in metal-ferroelectric junctions: A theoretical study. **Applied Physics Letters**, v. 92, 2008.

32. COHEN, R. E. Origin of ferroelectricity in perovskite oxides. **Nature**, v. 358, 1992.

33. KUMAR, M.; YADAV, K. L.; VARMA, G. D. Large magnetization and weak polarization in sol-gel derived BiFeO3 ceramics. **Materials Letters**, v. 62, p. 1159--1161, 2008.

34. OHYA, Y.; TANAKA, T.; TAKAHASHI, Y. Dielectric properties of lead zirconate titanate thin film fabricated on In2O3: Sn substrate by sol-gel method. **Jpn. J. Appl. Phys**, v. 32, p. 4163--4167, 1993.

35. GIERSBACH, M. et al. Piezoelectric properties of PZT thin films on metallic substrates. **Ferroelectrics**, v. 241, p. 175-182, 2000.

36. HARMAN, T. V. **Ferroelectric thin film development**. [S.l.]: [s.n.], 2003.

37. NAGARAJ, B.; AGGARWAL, S.; RAMESH, R. Influence of contact electrodes on leakage characteristics in ferroelectric thin films. **Journal of Applied Physics**, v. 90, p. 375, 2001.

38. LEE, E. G. et al. Zr/Ti ratio dependence of the deformation in the hysteresis loop of Pb (Zr, Ti) O3 thin films. **Journal of materials science letters**, v. 18, p. 2025-2028, 1999.

39. PINTILIE, L.; ALEXE, M. Metal-ferroelectric-metal heterostructures with Schottky contacts. I. Influence of the ferroelectric properties. **Journal of applied physics**, v. 98, 2005.

40. KOLASINSKI, K. K. **Surface science:** foundations of catalysis and nanoscience. [S.l.]: Wiley, 2012.

41. LÜTH, H. **Solid surfaces, interfaces and thin films**. [S.l.]: Springer Verlag, 2012.

42. VAN ZEGHBROECK, B. Principles of semiconductor devices. **Colorado University**, 2004.

43. IZYUMSKAYA, N. et al. Processing, structure, properties, and applications of PZT thin films. **Critical reviews in solid state and materials sciences**, v. 32, 2007.

44. DAWBER, M.; RABE, K. M.; SCOTT, J. F. Physics of thin-film ferroelectric oxides. **Reviews of modern physics**, v. 77, 2005.

45. PINTILIE, L. et al. Metal-ferroelectric-metal structures with Schottky contacts. II. Analysis of the experimental current-voltage and capacitance-voltage characteristics of Pb (Zr, Ti) O thin films. **Journal of applied physics**, v. 98, 2005.

46. KAO, K. C.; HWANG, W. **Electrical transport in solids:** with particular reference to organic semiconductors. [S.l.]: Taylor & Francis, 1979.

47. NAKAMURA, Y.; NAKASHIMA, S.; OKUYAMA, M. Improvement of ferroelectric properties of BiFeO3 thin films by postmetallization annealing and electric field application. **Journal of Applied Physics**, v. 105, 2009.

48. YANG, H. et al. Rectifying current-voltage characteristics of BiFeO3/ Nb-doped SrTiO3 heterojunction. **Applied Physics Letters**, v. 92, 2008.

49. SIMOES, A. Z. et al. Strain behavior of lanthanum modified BiFeO3 thin films prepared via soft chemical method. **Journal of Applied Physics**, v. 104, p. 104115--104115, 2008.

50. CHENG, Z. et al. A way to enhance the magnetic moment of multiferroic bismuth ferrite. **Journal of Physics D: Applied Physics**, v. 43, p. 242001, 2010.

51. LIN, Y. H. et al. Enhancement of ferromagnetic properties in BiFeO3 polycrystalline ceramic by La doping. **Applied physics letters**, v. 90, p. 172507--172507, 2007.

52. KHAN, M. A.; COMYN, T. P.; BELL, A. J. Leakage mechanisms in bismuth ferrite-lead titanate thin films on Pt/Si substrates. **Applied Physics Letters**, v. 92, 2008.

53. HU, G. D. et al. Effects of Gd substitution on structure and ferroelectric properties of BiFeO thin films prepared using metal organic decomposition. **Applied Physics Letters**, v. 91, p. 232909, 2007.

54. PINTILIE, L. et al. Ferroelectric polarization-leakage current relation in high quality epitaxial Pb (Zr, Ti) O3 films. **Physical Review B**, v. 75, 2007.

55. SCOTT, J. Data storage: Multiferroic memories. **Nature Materials**, v. 6, 2007.

56. EERENSTEIN, W.; MATHUR, N.; SCOTT, J. Multiferroic and magnetoelectric materials. **Nature**, v. 442, p. 759--765, 2006.

57. QI, X. et al. Epitaxial growth of BiFeO3 thin films by LPE and sol–gel methods. **Journal of magnetism and magnetic materials**, v. 283, p. 415--421, 2004.

58. CHU, Y. H. et al. Controlling magnetism with multiferroics. **Materials Today**, v. 10, p. 16--23, 2007.

59. WANG, Y. et al. Room-temperature saturated ferroelectric polarization in BiFeO ceramics synthesized by rapid liquid phase sintering. **Applied physics letters**, v. 84, p. 1731, 2004.

60. SINGH, S. K.; ISHIWARA, H. Reduced leakage current in BiFeO3 thin films on Si substrates formed by a chemical solution method. **Japanese journal of applied physics**, v. 44, p. L734--L736, 2005.

61. LEBEUGLE, D. et al. Very large spontaneous electric polarization in BiFeO3 single crystals at room temperature and its evolution under cycling fields. **Applied physics letters**, p. 022907--022907, 91 2007.

62. MISIRLIOGLU, I. B.; OKATAN, M. B.; ALPAY, S. P. Asymmetric hysteresis loops and smearing of the dielectric anomaly at the transition temperature due to space charges in ferroelectric thin films. **JOURNAL OF APPLIED PHYSICS**, v. 118, n. 3, 2010.

63. RAMESH, R.; SPALDIN, N. A. Multiferroics: progress and prospects in thin films. **Nature Materials**, v. 6, p. 21, 2007.

64. ZHAO, T. et al. Electrical control of antiferromagnetic domains in multiferroic BiFeO(3) films at room temperature. **NATURE MATERIALS**, v. 5, n. 10, p. 823, 2006.

65. ZECHES, R. J. et al. A Strain-Driven Morphotropic Phase Boundary in BiFeO3. **Science**, v. 326, p. 977, 2009.

66. FUJINO, S. et al. Combinatorial discovery of a lead-free morphotropic phase boundary in a thin-film piezoelectric perovskite. **APPLIED PHYSICS LETTERS**, v. 92, p. 202904, 2008.

67. SEIDEL, J. et al. Conduction at domain walls in oxide multiferroics. **NATURE MATERIALS**, v. 8, p. 229, 2009.

68. GUO, S. M. et al. Rectifying I-V characteristic of LiNbO3/Nb-doped SrTiO3 heterojunction. **Applied Physics Letters** , v. 89, p. 223506, 2006.

69. ARREDONDO, M. et al. Structural defects and local chemistry across ferroelectric--electrode interfaces in epitaxial heterostructures. **Journal of materials science**, v. 44, 2009.